NJC

ROYAL SOCIETY OF CHEMISTRY

PAPER

View Article Online
View Journal

Cite this: DOI: 10.1039/d1nj01491a

Heteroleptic enantiopure Pd(II)-complexes derived from halogen-substituted Schiff bases and 2-picolylamine: synthesis, experimental and computational characterization and investigation of the influence of chirality and halogen atoms on the anticancer activity†

Nazanin Kordestani,[a] Hadi Amiri Rudbari, *[a] Isabel Correia, [b] Andreia Valente, *[c] Leonor Côrte-Real,[c] Mohammad Khairul Islam,[d] Nicola Micale,[e] Jason D. Braun, [f] David E. Herbert, [f] Nikolay Tumanov, [g] Johan Wouters[g] and Mohammed Enamullah *[d]

Seven enantiomeric pairs of palladium complexes, [Pd(pic)(*R* or *S*)-*N*-1-(phenyl)ethyl-2,4-X_1,X_2-salicylaldiminate)]NO_3, [Pd(pic)(*R* or *S*)]NO_3 (X_1 = X_2 = Cl, Br, I, H; X_1/X_2 = Br/Cl), were synthesized by the reaction of enantiopure halogen-substituted Schiff bases (*R* or *S*)-*N*-1-(phenyl)ethyl-2,4-X_1,X_2-salicylaldimine with [Pd(pic)Cl_2] (pic = 2-picolylamine). The composition and structure of the complexes were confirmed by means of FT-IR, ^{1}H NMR and ^{13}C NMR spectroscopy, elemental analysis and X-ray crystallography. The electronic structure of the reported complexes was investigated using UV–vis absorption and electronic circular dichroism (ECD) spectroscopy, complemented by DFT/TDDFT modelling. To investigate the effect of chirality and different halogen substituents on the anticancer activity of the complexes, the cytotoxic activity of all fourteen complexes was tested in the human breast cancer cell lines MDA-MB-231 and MCF-7 at 24 h using the colorimetric MTT assay. Also, the cell death mechanism was assessed using the annexin V/propidium iodide (AV/PI) cytometry-based assay.

Received 26th March 2021,
Accepted 16th April 2021

DOI: 10.1039/d1nj01491a

rsc.li/njc

Introduction

Chirality is an important tool for modern drug discovery as the molecular recognition of chiral biological targets can provide essential insights into the design of new active drugs.[1] Indeed, many drugs currently on the market are chiral, and their therapeutic activity depends on the stereospecific recognition of biomolecules.[2] Besides, the biological activity of enantiomers can also differ drastically in terms of toxicity and pharmacokinetics. Indeed, one of them may be beneficial, whereas the other may be harmful or inactive. This is valid not only for organic drugs but also for metallodrugs, in which the enantiomeric resolution becomes necessary for their medicinal applicability.[3] An example of the latter is oxaliplatin, one of the most commonly used and active chemotherapeutic drugs utilized in oncology nowadays, that contains the chiral ligand 1*R*,2*R*-cyclohexane-1,2-diamine (Fig. 1). This platinum-based anticancer compound is more biologically active and chemically reactive than its enantiomer (Fig. 1) containing the ligand 1*S*,2*S*-cyclohexane-1,2-diamine.[4] Other examples of potent chiral antineoplastic agents are the platinum drugs heptaplatin (administered as a single enantiomer) and lobaplatin (that is used as a ~1:1 diastereomeric mixture SSS, RRS).[5]

In addition, halogens (fluorine (F), chlorine (Cl), bromine (Br), and iodine(I)) as the substituents of the pharmacologically

[a] Department of Chemistry, University of Isfahan, Isfahan 81746-73441, Iran. E-mail: h.a.rudbari@sci.ui.ac.ir, hamiri1358@gmail.com
[b] Centro de Química Estrutural, Departamento de Engenharia Química, Instituto Superior Técnico, Av. Rovisco Pais 1, 1049-001 Lisboa, Portugal
[c] Centro de Química Estrutural and Departamento de Química e Bioquímica, Faculdade de Ciências, Universidade de Lisboa, Campo Grande, 1749-016 Lisboa, Portugal. E-mail: amvalente@fc.ul.pt
[d] Department of Chemistry, Jahangirnagar University, Dhaka1342, Bangladesh. E-mail: enamullah@juniv.edu
[e] Department of Chemical, Biological, Pharmaceutical and Environmental Sciences, University of Messina, Viale Ferdinando Stagno D'Alcontres 31, I-98166 Messina, Italy
[f] Department of Chemistry, University of Manitoba, Winnipeg, Manitoba R3T 2N2, Canada
[g] Department of Chemistry, Namur Institute of Structured Matter, University of Namur, 5000 Namur, Belgium

† Electronic supplementary information (ESI) available. CCDC 1989598 and 2007895. For ESI and crystallographic data in CIF or other electronic format, see DOI: 10.1039/d1nj01491a

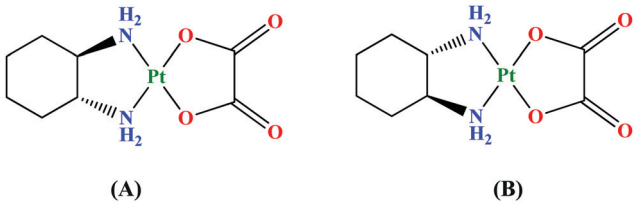

Fig. 1 Enantiomers of the Pt(II)-based drug oxaliplatin with chiral ligands. (A) 1*R*,2*R*-cyclohexane-1,2-diamine (oxaliplatin in clinical use); (B) 1*S*,2*S*-cyclohexane-1,2-diamine (not in clinical use).

active ligands are widely used in drug design.[6] Approximately 50% of molecules in high-throughput screening are halogenated and around 40% of drugs currently on the market or in clinical trials are halogenated.[7] The large proportion of halogenated drugs in the clinic and clinical trials implies the existence of halogen bonds in drug–target complexes.[7,8] A halogen bond (XB) in biomolecules can be referred to as a short C–X···D–Z interaction, where D is a halogen bond donor; C–X is a carbon-bonded chlorine, bromine, or iodine; D–Z is a carbonyl, hydroxyl, thiol, aromatic ring, charged carboxylate, phosphate group or amine; and the X···D distance is less than or equal to the sum of the respective van der Waals radii.[9] Halogen bonds (XBs) are attracting increasing attention in the design of drugs due to their ability to improve the binding affinity towards the intended target and tune the ADME/T (absorption, distribution, metabolism, excretion, and toxicity) profile of the resulting compounds.[8,10] Halogen bonding can also be exploited for designing metal complex ligands or biologically active organic compounds to overcome the drug-resistance phenomenon.[8,11] On the basis of the structural and thermodynamic analogy between platinum(II) and palladium(II) complexes,[12] a variety of studies on palladium(II) derivatives as potential anticancer drugs have been performed.[13] The aquation and ligand-exchange rates of the Pd(II)-complexes are about 10^5 times faster than those of the Pt(II) analogues. Moreover, the Pd(II)-complexes have overall a better solubility compared to that of the Pt(II) complexes.[14] Therefore, it seems that at least some Pd(II)-complexes may have considerable potential for cancer therapy. It was recently reported that Pd(II)-complexes have significant anticancer activity and lower toxicity compared with some clinically used chemotherapeutics.[15] However, less attention has been focused on the synthesis and characterization of enantiopure Pd(II)-complexes endowed with biological activity.[16] Indeed, according to our search in the literature, there are no reports about the synthesis of heteroleptic enantiopure Pd(II)-complexes for biological investigations.

Schiff bases are useful chelating ligands for metal ions, resulting in complexes with different physical and chemical properties.[17] Thus, the metal complexes of Schiff bases have been extensively designed and investigated for biomedical applications, such as antitumor,[18] anti-inflammatory,[19] antibacterial[20] and antifungal[21] activities. Recently, our group reported that Pd(II) and V(V) complexes containing chiral Schiff base ligands exhibited unique biological characteristics.[22]

Based on the above discussion, and in an attempt to find new potent anticancer agents, together with the consideration that pyridine moieties, Schiff base ligands, halogenation and chirality are attractive in medicinal and pharmaceutical chemistry, fourteen optically pure chiral heteroleptic Pd(II)-complexes (*i.e.* seven enantiomeric pairs) were designed, synthesized and characterized, with the aim of exploring their potential stereospecific anticancer activities.

The enantiopure Schiff bases, (*R* or *S*)-*N*-1-(phenyl)ethyl-2,4-X^1,X^2-salicylaldimine (X^1, X^2 = Cl, Br, I), were also recently used for the synthesis of pseudotetrahedral chiral copper(II) complexes in our research group.[23] For the synthesis of the heteroleptic Pd(II)-complexes, we also used a bidentate amine ligand having a heteroaromatic nitrogen base (2-picolylamine) that possesses π-accepting properties, which is believed to be involved in the π–π stacking effects with purine and pyrimidine bases. In this respect, it is very interesting to note that Farrell *et al.*[24] found a considerable increase in the cytotoxicity of *trans*-[Pt(py)$_2$Cl$_2$] complexes in comparison to inactive *trans*-[Pt(NH$_3$)$_2$Cl$_2$] by introducing aromatic nitrogen ligands. Also, a systematic variation of the N-heterocyclic ligands in

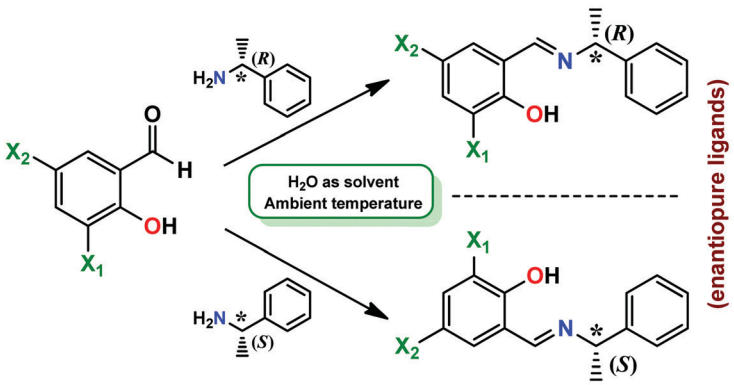

X_1	X_2	
H	H	**HR1**
H	Cl	**HR2**
H	Br	**HR3**
Cl	Cl	**HR4**
Br	Br	**HR5**
I	I	**HR6**
Br	Cl	**HR7**

X_1	X_2	
H	H	**HS1**
H	Cl	**HS2**
H	Br	**HS3**
Cl	Cl	**HS4**
Br	Br	**HS5**
I	I	**HS6**
Br	Cl	**HS7**

Fig. 2 Synthesis of the enantiopure Schiff bases, (*R* or *S*)-*N*-1-(phenyl)ethyl-2,4-X_1,X_2-salicylaldimine.

compounds of the formula *cis*-$[Pt(NH_3)_2(Am)Cl]^+$ (where Am denotes a N-heterocyclic ligand), by Lippard *et al.*, resulted in the monofunctional DNA-binding phenanthriplatin, which showed greater efficacy than cisplatin and oxaliplatin in established human cancer cells and revealed a distinct pattern of activity.[25]

Results and discussion

Synthesis, stereochemistry and spectroscopic studies

The condensation of halogen-substituted salicylaldehydes with enantiopure (*R*)-(+)-α-methylbenzylamine or (*S*)-(−)-α-methylbenzylamine yields the enantiopure Schiff bases (*R* or *S*)-*N*-1-(phenyl)ethyl-2,4-X_1,X_2-salicylaldimine (**HR1–7** and **HS1–7**) (Fig. 2). The purity and identity of the Schiff bases were established using elemental analysis, and multinuclear NMR and FT-IR spectroscopies.[23] The reaction of $[Pd(pic)Cl_2]$ (pic = 2-picolylamine) with these asymmetric *N*^*O*-chelating Schiff base ligands affords the asymmetric optically active palladium complexes (Fig. 3).

Four-coordinated metal compounds with two asymmetrical bidentate ligands in a square-planar geometry afford a mixture of two geometrical isomers, **A** and **B**, as shown in Fig. 4. In isomer **A**, the oxygen atom of the Schiff base ligand is in front of the $-NH_2$ group of 2-picolylamine, while in isomer **B**, the oxygen atom of the Schiff base ligand is in front of the $-N_{py}$ group of 2-picolylamine (Fig. 4). However, a mixture of the two isomers was not obtained in the synthesis due to steric hindrance between the pyridine and $-CH(C_6H_6)CH_3$ groups. Only conformation **A** can be prepared from the reaction of $[Pd(pic)Cl_2]$ with the chiral Schiff base ligands. Configuration **A** was confirmed using X-ray crystallography in **[Pd(pic)*R*3]NO_3** and also racemic **[Pd(pic)*rac*2]NO_3**.

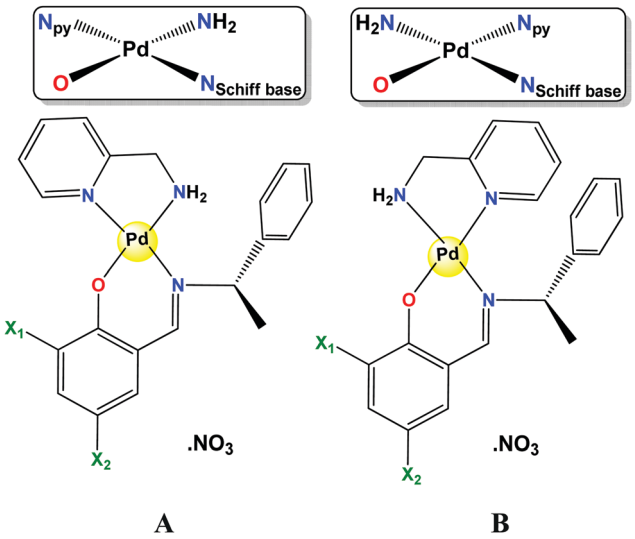

Fig. 4 Geometrical isomers for the synthesized Pd(II)-complexes that may form.

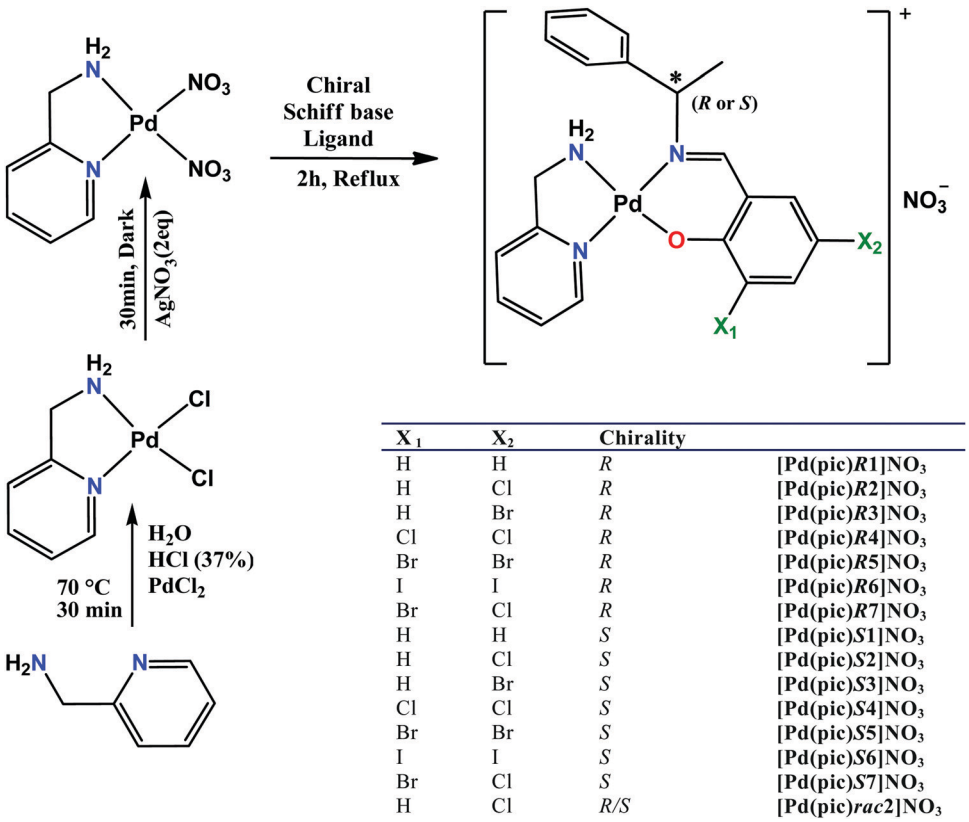

X_1	X_2	Chirality	
H	H	*R*	**[Pd(pic)*R*1]NO_3**
H	Cl	*R*	**[Pd(pic)*R*2]NO_3**
H	Br	*R*	**[Pd(pic)*R*3]NO_3**
Cl	Cl	*R*	**[Pd(pic)*R*4]NO_3**
Br	Br	*R*	**[Pd(pic)*R*5]NO_3**
I	I	*R*	**[Pd(pic)*R*6]NO_3**
Br	Cl	*R*	**[Pd(pic)*R*7]NO_3**
H	H	*S*	**[Pd(pic)*S*1]NO_3**
H	Cl	*S*	**[Pd(pic)*S*2]NO_3**
H	Br	*S*	**[Pd(pic)*S*3]NO_3**
Cl	Cl	*S*	**[Pd(pic)*S*4]NO_3**
Br	Br	*S*	**[Pd(pic)*S*5]NO_3**
I	I	*S*	**[Pd(pic)*S*6]NO_3**
Br	Cl	*S*	**[Pd(pic)*S*7]NO_3**
H	Cl	*R/S*	**[Pd(pic)*rac*2]NO_3**

Fig. 3 Synthetic route to enantiopure Pd(pic)–enantiopure Schiff bases complexes.

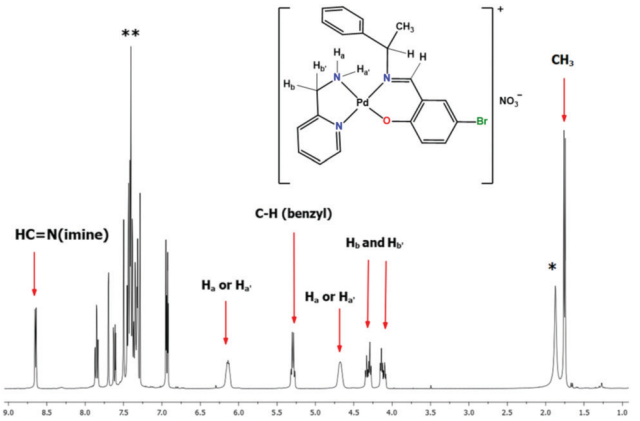

Fig. 5 ^{1}H NMR spectrum of [Pd(pic)*R*3]NO_3 in $CDCl_3$ at room temperature (** peak for $CDCl_3$ and * peak for water in $CDCl_3$).

Due to the above discussion, for our synthesized Pd(II) chiral complexes, the existence of the two isomers in equimolar or different quantities generally should produce two sets of signals for each proton in the related ^{1}H NMR spectrum, which allows us to distinguish the isomers from each other. However, in this case, the ^{1}H NMR spectrum of all newly synthesized Pd(II)-complexes showed only one pattern of signals for each proton, as can be seen in Fig. 5 for **[Pd(pic)*R*3]NO_3**. Then, the ^{1}H NMR spectrum confirms the presence of a single isomer, **A**, for the complexes in solution.

Both the ^{1}H and ^{13}C NMR spectra of the complexes are consistent with the assigned structures (for example: the ^{1}H NMR of **[Pd(pic)*R*3]NO_3** in Fig. 5). The resonance signal corresponding to the phenolic (OH) proton disappears in the complex spectra, indicating the deprotonation and coordination of oxygen to the Pd(II) ion. In the ligands, the HC = N proton appears as a sharp singlet at 8.15–8.45 ppm, while after complexation, it is converted into a doublet that shifted downfield by 0.2–1.0 ppm.[23] The conversion of the singlet into a doublet following complexation can be attributed to coupling between the H1 and H4 protons (Fig. 6 and 7). The Pd(II)-complexes are rigid, and therefore, the imine hydrogen is located

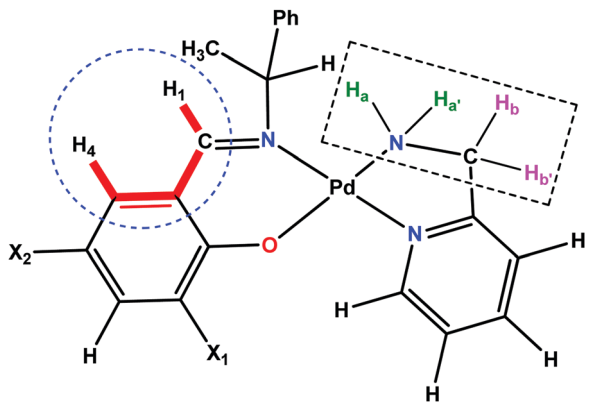

Fig. 6 Long-range coupling (between H1 and H4) and diastereotopic protons (H_a, $H_{a'}$, H_b and $H_{b'}$).

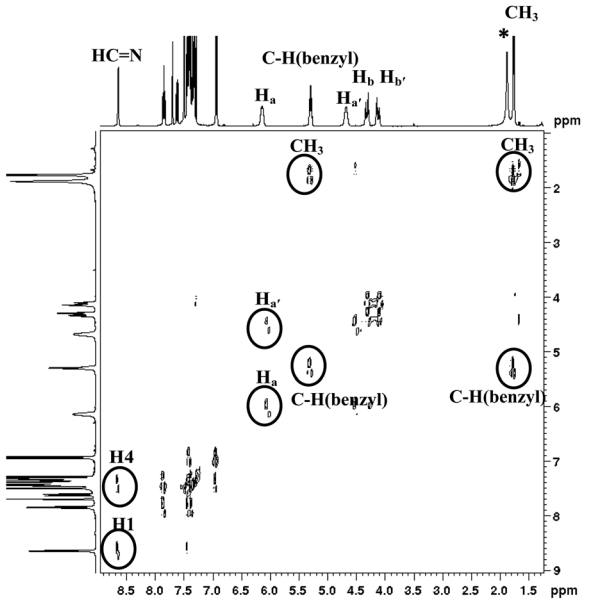

Fig. 7 ^{1}H–^{1}H-2D COSY NMR spectra of [Pd(pic)*R*3]NO_3 in $CDCl_3$ at room temperature.

close to H4 and a long-range coupling is observed as seen in the ^{1}H–^{1}H-2D COSY NMR spectra (Fig. 7). Such a long-range coupling was previously observed in the Pd(II)-complexes of the *R*/*S*-(1-phenylethylimino)methylnaphtalen-2-ol) ligand.[22a]

The protons of the amino group of 2-picolylamine show two multiplets at about 6.0 and 4.5 ppm after the coordination of [Pd(pic)Cl_2] with the Schiff base ligands. The presence of two signals for the two protons of the amino group is due to the lack of any symmetry elements in the complexes. Then, the H_a and $H_{a'}$ protons are diastereotopic and show two sets of multiplets. This connection between the H_a and $H_{a'}$ protons also is observed in the ^{1}H–^{1}H-2D COSY NMR spectra (Fig. 5 and 7). Similarly, the –CH_2 protons of 2-picolylamine show two separate triplet of doublet signals at about 3.8 and 4.3 ppm that shifted upfield after the coordination of the Schiff base ligand with $[Pd(pic)]^{2+}$. The signal of benzylic hydrogen, (C*H*(CH_3)(C_6H_6)), appears as a quartet at about 5.1–5.4 ppm, shifted downfield by 0.5–0.8 ppm with respect to the free Schiff base. The methyl group of the ligand in the complexes shows a doublet at about 1.6 ppm that remains nearly unshifted with respect to the free Schiff base ligands. In the ^{1}H–^{1}H-2D COSY NMR spectra (Fig. 7), the connection between the methyl group protons and benzylic hydrogen is also due to the vicinity of these two classes of protons.

The infrared spectra of the Pd(II)-complexes feature a very strong band at 1612–1620 cm^{-1} that is consistent with ν(CH=N).[22a] The shift of the imine band to lower wavenumbers upon complexation with respect to the free ligands suggests coordination *via* the imine nitrogen atoms.[22a] Then, the most relevant feature of the IR spectra of the ligands and complexes is the red shift of the ν(CH=N) bands upon the coordination of ligands to the metal ions.[26] This feature can be explained by the withdrawal of electrons from the nitrogen atom to the metal ion

due to the coordination process. The presence of several medium intensity bands in the range of 2910–3100 cm^{-1} is due to the existence of the C–H stretching vibrations of aliphatic and aromatic protons. The strong and sharp band at $\sim$1383 cm^{-1} is the characteristic of ionic nitrate, consistent with an outer sphere counter ion.[27]

X-ray and optimized structures

The chirality of the Pd(II)-complexes was confirmed by single crystal X-ray diffraction analysis for the enantiopure **[Pd(pic)*R*3]NO_3** and racemic **[Pd(pic)*rac*2]NO_3** complexes. Single crystals suitable for X-ray diffraction studies were obtained by the slow diffusion of diethyl ether into a DMF solution of the complexes. A view of the molecular structures with the common atom numbering scheme is shown in Fig. 8, while the selected bond lengths and angles are collected in Table 1. As shown in Fig. 8, it is only possible to form the isomer **A** for the Pd(II)-complexes. The crystal packing of **[Pd(pic)*rac*2]NO_3** is centrosymmetric ($P\bar{1}$), and therefore, the crystallized compound is a racemic mixture of the two enantiomers **[Pd(pic)*R*2]NO_3** and **[Pd(pic)*S*2]NO_3**. The enantiomer with *S*-conformation on C(8), **[Pd(pic)*S*2]NO_3**, is shown in Fig. 8. The complex **[Pd(pic)*R*3]NO_3** crystallizes in the space group $P2_12_12_1$, a non-centrosymmetric unit cell, with a Flack parameter[28] of 0.034(8) that confirms the formation of enantiopure crystals consistent with the model shown in Fig. 8. The chiral center in the Schiff base ligands has the *R*-configuration, which is consistent with the chirality of the ligand precursors used in the synthesis.

The crystallographic data reveal that Pd(II) is four-coordinated in both structures, **[Pd(pic)*rac*2]NO_3** and **[Pd(pic)*R*3]NO_3**, by the phenolate oxygen and imine nitrogen atoms from the Schiff bases and two nitrogen atoms from the 2-picolylamine (pic). The dihedral angles between the two coordinating planes O(1)–Pd(1)–N(1) and N(2)–Pd(1)–N(3) are very small, θ = 0.45° in **[Pd(pic)*S*2]NO_3** of **[Pd(pic)*rac*2]NO_3** and 2.15° in **[Pd(pic)*R*3]NO_3**, indicating that the geometry around the metal ion is slightly distorted square planar.[29–31]

The bond distances and angles are very similar in **[Pd(pic)*rac*2]NO_3** and **[Pd(pic)*R*3]NO_3** as reported in Table 1. This similarity can also be confirmed by overlaying the cationic part of $[Pd(pic)R3]^+$ and $[Pd(pic)R2]^+$ of **[Pd(pic)*rac*2]NO_3**. As shown in Fig. S1 (ESI†), most of the atom sites overlap well. The most significant difference is observed at the orientation of the $-CH(CH_3)(C_6H_5)$ group, which can result from the intermolecular interactions.

The Pd(1)–N(2) bond lengths in both the structures (2.047(2) Å for **[Pd(pic)*rac*2]NO_3** and 2.051(2) Å for **[Pd(pic)*R*3]NO_3**) are longer than the Pd(1)–N(3) (aromatic N) bond lengths (2.028(2) Å for **[Pd(pic)*rac*2]NO_3** and 2.015(2) Å for **[Pd(pic)*R*3]NO_3**) and comparable to the analogous Pd(II)-complexes.[32] The Pd(1)–O(1) (1.9811(18) Å for **[Pd(pic)*rac*2]NO_3** and 1.971(2) Å for **[Pd(pic)*R*3]NO_3**) and Pd(1)–N(1) (2.016(2) Å for **[Pd(pic)*rac*2]NO_3** and 2.022(2) Å for **[Pd(pic)*R*3]NO_3**) bond lengths are similar to those reported for the related complexes.[22a,31] The imine bond lengths (1.292(4) Å and 1.288Å for **[Pd(pic)*rac*2]NO_3** and **[Pd(pic)*R*3]NO_3**, respectively) and bond angles for C(7)–N(1)–C(8) (118.5(2)° and 118.28(2)° for **[Pd(pic)*rac*2]NO_3** and **[Pd(pic)*R*3]NO_3**, respectively) confirm the double bond characters, with the sp^2 hybridization of the imino nitrogen atom.[22a,26] The six-membered chelate ring formed by the salicylaldimine fragment of the ligand is not planar. The Pd atom is displaced from the plane constituted by the remaining five atoms (0.405 Å for **[Pd(pic)*R*3]NO_3** and −0.133 Å for **[Pd(pic)*rac*2]NO_3**). Thus, the chelate ring is folded along the O(1) and N(1) line in the O(1)–C(1)–C(2)–C(7)–N(1)–Pd(1) ring and has a half-chair like conformation. Due to the formation of a five-membered chelate ring, the N(2)–Pd(1)–N(3) angle is

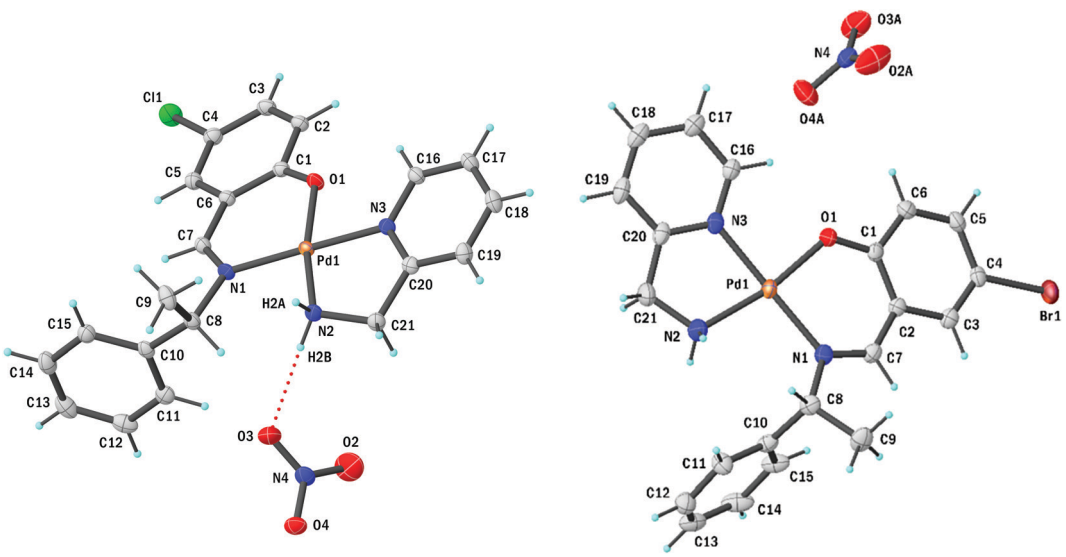

Fig. 8 Perspective view of the cationic Δ-**[Pd(pic)*S*2]NO_3** (left) and **Λ-[Pd(pic)*R*3]NO_3** (right) showing their asymmetric unit. Thermal ellipsoids are drawn at the 50% probability level, while the hydrogen size is arbitrary. The counter ion (NO_3^-) for **Λ-[Pd(pic)*R*3]NO_3** is disordered over two sites and refined with site occupancy factors 0.675 : 0.325. Only the major component of the disordered NO_3^- group is shown.

Table 1 Experimental and calculated bond lengths (Å) and angles (°) in the cationic Pd(II)-complexes

X-ray structures			DFT optimized structures		
Bond lengths (Å) and angles (°)	Δ-[Pd(pic)*rac*2]$^+$	Λ-[Pd(pic)*R*3]$^+$	Λ-[Pd(pic)*R*3]$^{+a}$	Δ-[Pd(pic)*R*3]$^{+a}$	Λ-[Pd(pic)*R*3]$^{+b}$
Pd–N(1)	2.016(2)	2.022(2)	2.0445	2.05096	2.1500
Pd–N(2)	2.047(2)	2.051(2)	2.1116	2.10812	2.1234
Pd–N(3)	2.028(2)	2.015(2)	2.0596	2.06102	2.0661
Pd–O(1)	1.9811(18)	1.971(2)	1.9867	1.98841	1.9991
C(7)–N(1)	1.292(4)	1.288(4)	1.3182	1.32155	1.3174
O(1)–Pd(1)–N(3)	87.95(8)	87.66(8)	87.90	87.51234	87.94
O(1)–Pd(1)–N(1)	92.84(8)	92.36(8)	93.11	92.81871	93.03
N(3)–Pd(1)–N(1)	179.18(8)	178.01(12)	178.96	178.45179	179.02
O(1)–Pd(1)–N(2)	168.74(9)	169.23(9)	167.94	166.99694	167.78
N(3)–Pd(1)–N(2)	80.80(9)	81.61(10)	80.08	79.61692	79.88
N(1)–Pd(1)–N(2)	98.41(9)	98.40(10)	98.91	100.09668	99.14
C(7)–N(1)–C(8)	118.5(2)	118.28(2)	119.36	115.67320	119.76
θ^c (°)	0.45	2.16	0.98	2.35	1.08

[a] Calculated at B3LYP/SDD. [b] B3LYP/LANL2DZ. [c] Dihedral angle (θ/°) between the two coordinating planes O(1)–Pd(1)–N(1) and N(2)–Pd(1)–N(3).

80.81° and 81.61° in **[Pd(pic)*rac*2]NO$_3$** and **[Pd(pic)*R*3]NO$_3$**, respectively.[32,33] The pyridine moiety and the planar coordination sphere are nearly co-planar, as indicated by the O(1)–Pd(1)–N(3)–C(16) torsion angle of only 11.6° for both the structures.

The X-ray molecular structures for the four-coordinated non-planar metal(II)-complexes with asymmetric bidentate chiral ligands exhibit induced chirality at the metal center and provide two opposite configured Δ- and Λ-diastereomers.[29–31] Hence, based on the dihedral angle θ = 2.15° and the ligand folding angles ϕ_1 = 16.31° (angle between the planes of N(1)–Pd(1)–O(1) and the salicylal ring, upward plane with respect to the O(1)–N(1)–Pd(1)–N(2)–N(3) plane) and ϕ_2 = 5.80° (angle between the planes of N(2)–Pd(1)–N(3) and the phenyl ring, downward plane with respect to the O(1)–N(1)–Pd(1)–N(2)–N(3) plane), the structure for **[Pd(pic)*R*3]NO$_3$** could be best described as a Λ-diastereomer (Fig. 8).[29b] The DFT optimized structures for the diastereomeric pairs **Λ-[Pd(pic)*R*3]$^+$** and **Δ-[Pd(pic)*R*3]$^+$** (Fig. 9) show that the former one is relatively more stable by 58.36 kcal mol^{-1}, in parallel to the X-ray structural results. In fact, the X-ray molecular structures along with the DFT calculations reveal, in general, the preferred formation of the Λ-diastereomer in most enantiopure crystals of *R*-ligated complexes and the Δ-diastereomer in most enantiopure crystal structures of the *S*-ligated complexes, in the context of induced chirality at the metal and diastereoselection phenomenona.[29–31] The optimized structures for the enantiomeric pairs **Λ-[Pd(pic)*R*3]$^+$** and **Δ-[Pd(pic)*S*3]$^+$** are essentially equienergetic (Fig. S2, ESI†). Some selected bond lengths and angles in the optimized structures are listed in Table 1 and are comparable to the X-ray parameters obtained for **Λ-[Pd(pic)*R*3]NO$_3$** and **Δ-[Pd(pic)*rac*2]$^+$**. The dihedral angles for the optimized structures are very small (0.98 and 2.35°) and close to the X-ray values (Table 1).

As shown in Fig. S3 and S4 (ESI†), the crystal packing for these two structures is different because of the existence of a racemic mixture in the crystal packing of **[Pd(pic)*rac*2]NO$_3$** and an enantiopure compound in the crystal packing of **[Pd(pic)*R*3]NO$_3$**. The most important intermolecular interaction is O$_2$N–O···H–NH in **[Pd(pic)*rac*2]NO$_3$**, while O$_2$N–O···H–NH and O$_2$N–O···H–C in **[Pd(pic)*R*3]NO$_3$** (Table S1). The cationic parts of the **[Pd(pic)*R*3]NO$_3$** molecule, **[Pd(pic)*R*3]$^+$**, interact with each other *via* N–H···O$_2$N–O and C–H···O$_2$N–O hydrogen bonds, while the crystal packing of **[Pd(pic)*rac*2]NO$_3$** adopts a $R_4^4(12)$ dimer ring (using a graph set notation), where $R_d^a(r)$ is a ring of *r* atoms involving a acceptors and d donors[34] due to the existence of the racemic mixture (Fig. S3 and S4, ESI†). Beyond these strong interactions, there are several other weak interactions in the crystal packing of both complexes (see Table S1, ESI†). Therefore, the above discussion indicates that the most and the strongest intermolecular interactions in the crystal packing of both complexes occur between the cationic unit and the NO_3^- counter ion (Table S1 and Fig. S3, S4, ESI†), reflecting the importance of the NO_3^- units to the stabilization of the crystal structure.

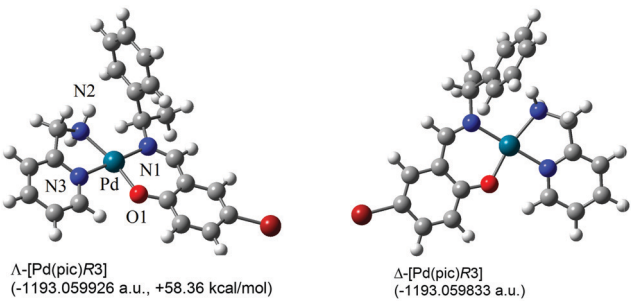

Fig. 9 DFT optimized structures (gas phase) for the diastereomeric pair **Λ-[Pd(pic)*R*3]$^+$** and **Δ-[Pd(pic)*R*3]$^+$**, calculated at B3LYP/SDD.

Hirshfeld surface analyses

In order to quantify the various intermolecular interactions, Hirshfeld surfaces (HSs) and their associated fingerprint plots were calculated using Crystal Explorer.[35] The HSs of **[Pd(pic)*S*2]NO$_3$** and **[Pd(pic)*R*3]NO$_3$** with their fingerprint plots are illustrated in Fig. S5 (ESI†), showing the surfaces that have been mapped over a d_{norm} range of −0.5 to 1.2 Å. The percentages of contributions to various types of contacts in the fingerprint plots are summarized in Fig. S6 (ESI†). It should be noted that due to the similarity in the crystal packing of the two enantiomeric complexes (**[Pd(pic)*R*2]NO$_3$** and **[Pd(pic)*S*2]NO$_3$**)

in the structure of **[Pd(pic)*rac*2]NO_3**, only **[Pd(pic)*S*2]NO_3** was investigated and reported in this section (see the ESI† for more details and also Fig. S7).

Experimental and calculated UV–vis and ECD spectra

The UV–vis absorption spectra were recorded in dichloromethane solutions for all complexes and show consistent similarities along the series (with *R* or *S*-ligands) with little changes in the band maxima (Fig. 10). All spectra show strong bands/shoulders below *ca.* 330 nm with two maxima (λ_{max}) at 250–260 nm and 280–290 nm, assigned as the intra-ligand π → π* and n → π* transitions (LL), respectively. The spectra show less intense broad bands at 350–500 nm (λ_{max} = 380–406 nm), assigned as the metal-to-ligand charge-transfer (MLCT) transitions.[36,37] The spectra also show a very weak and broad band in the visible region (450–600 nm; Fig. 10, inset), attributed to the metal-centered d–d transitions.[36] Indeed, the ligand-field parameters for the square planar complexes are relatively high, which overlap with the nearby strong MLCT band, and thus, the forbidden d–d transition bands are not separately visible (Fig. 10, inset). The n → π* and MLCT bands shift to lower energy from 278 and 380 nm (H, H) to 284 and 395 nm (Cl, Cl) upon substitution with increasing electronegative halogen atoms on the salicylal ring (Fig. 11). Here, the destabilization of metal–ligand interactions with halogen substituents weakens both the n → π* and MLCT bands and results in a hypsochromic shift of *ca.* 6 and 15 nm, respectively. The results suggest that the later band is relatively more charge-transfer in nature (Fig. 11).[37]

The electronic circular dichroism (ECD) spectra for all complexes in dichloromethane (Fig. 12) show consistent similarities for each enantiomeric pair along the series. The spectra show several bands with opposite Cotton effects, associated with the different electronic transitions as discussed in the UV–vis spectra. The observed mirror–image relationships of the ECD spectra indicate the enantiopurity or enantiomeric excess of *R* and *S*-ligated complexes in solution. The spectral data for the enantiomeric pairs, for example, **[Pd(pic)*R*3]NO_3** and **[Pd(pic)*S*3]NO_3**, are characterized by the following series of bands (sign and strength) at *ca.* 400 nm (±, weak), 278 nm (±, weak) and 255 nm (±, strong), respectively.

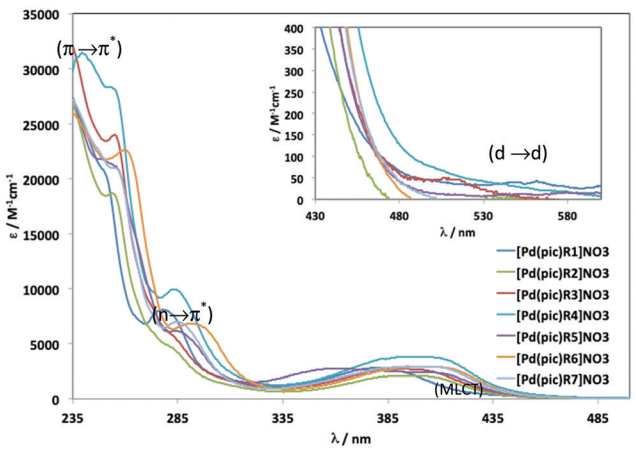

Fig. 10 UV–vis spectra for the Pd(pic)-complexes with *R*-ligands (*ca.* 0.022–0.083 mM) in dichloromethane at 25 °C.

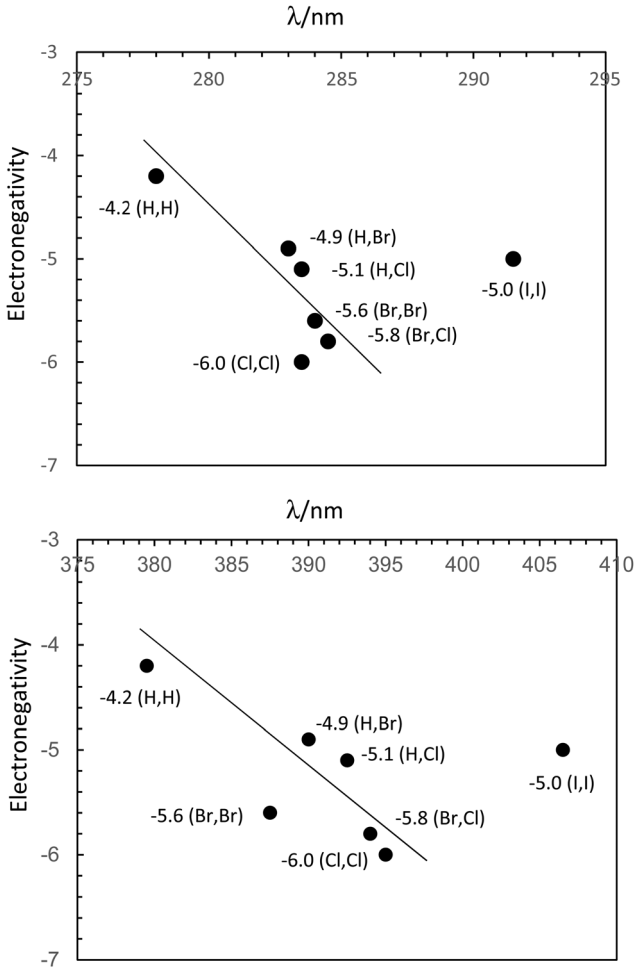

Fig. 11 Shifts of the n → π* (top) and MLCT (bottom) bands maxima with different substituents on the salicylal-ring in Pd(pic)-complexes with *R*-ligands (*ca.* 0.022–0.083 mM) in dichloromethane at 25 °C.

We calculated the UV–vis spectra for the diastereomeric pair **Λ-[Pd(pic)*R*3]$^+$/Δ-[Pd(pic)*R*3]$^+$**, which are identical (Fig. S8, ESI†) and correspond well to the experimental spectra with little shifts in the bands' maxima (Fig. 13). The calculated ECD spectra for the diastereomeric pair **Λ-[Pd(pic)*R*3]$^+$/Δ-[Pd(pic)*R*3]$^+$** and the enantiomeric pair **Λ-[Pd(pic)*R*3]$^+$/Δ-[Pd(pic)*S*3]$^+$** show the expected mirror–image relationships (Fig. S14 and S9 in ESI†). The calculated spectra exhibit different bands with opposite Cotton effects and correspond well to the experimental spectra with little shifted band maxima (Fig. 14), as reported in the related complexes.[29–31] Some selected and simplified assignments on the calculated UV–vis spectra are made on the basis of the orbital and population analyses for **Λ-[Pd(pic)*R*3]$^+$** and data are listed in Table 2. Again, the data are similar to the experimental results (Table 2). The band at 373 nm with a significant oscillator strength, 0.0513 (*f*), arises mainly from a combination of the metal–metal and metal–ligand electronic transitions with the highest MO

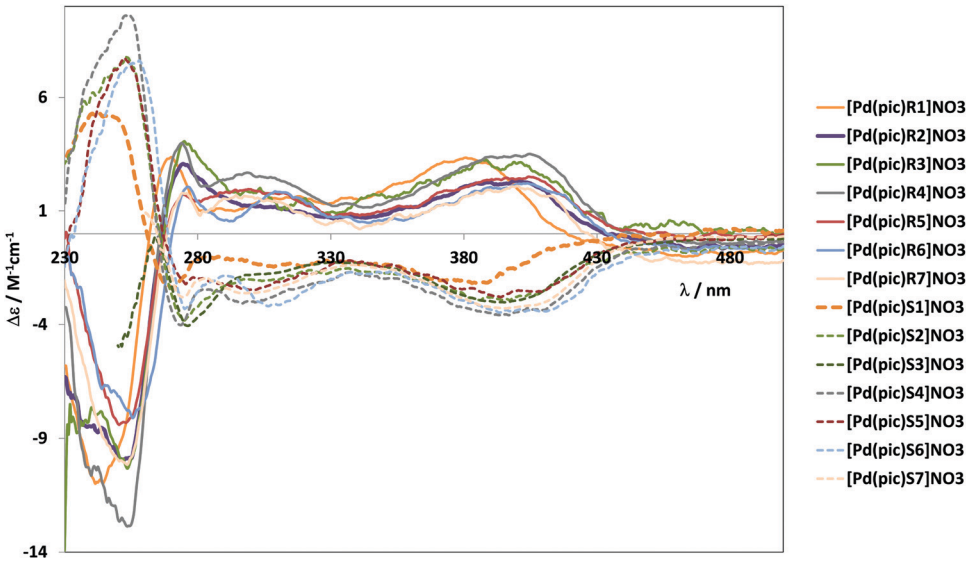

Fig. 12 ECD spectra for all enantiomeric pairs of **[Pd(pic)(*R*)]NO_3** and **[Pd(pic)(*S*)]NO_3** (*ca.* 0.20–0.30 mM) complexes in dichloromethane at 25 °C (cell path length: 2.0 mm).

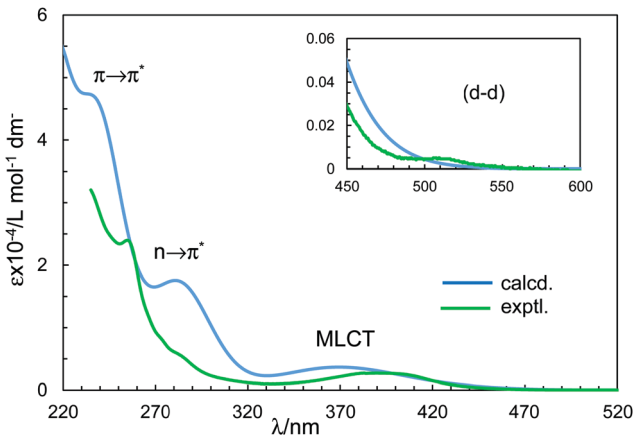

Fig. 13 Experimental spectrum for **[Pd(pic)*R*3]NO_3** (*ca.* 0.022 mM) in dichloromethane at 25 °C. The calculated spectrum for **[Λ-Pd(pic)*R*3]$^+$**, calculated at B3LYP/SDD with PCM in dichloromethane (Gaussian band shape with an exponential half-width, σ = 0.33 eV).

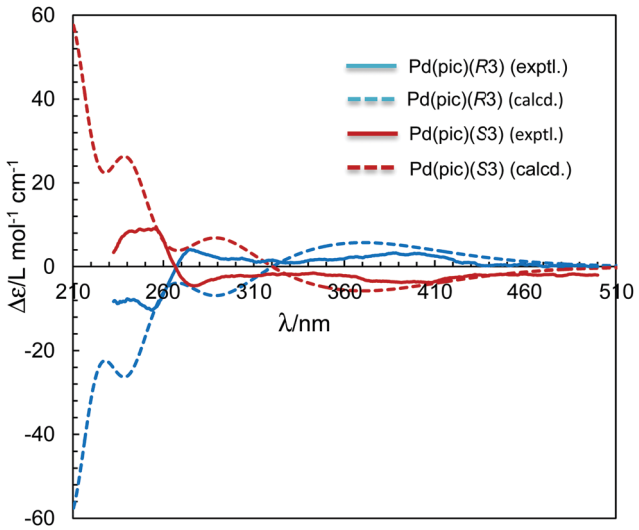

Fig. 14 Experimental ECD spectra for the enantiomeric pair **[Pd(pic)*R*3]NO_3** and **[Pd(pic)*S*3]NO_3** (*ca.* 0.20 mM and 2 mm optical path) in dichloromethane at 25 °C. The calculated ECD spectra for [Λ-Pd(pic)*R*3]$^+$ and [Δ-Pd(pic)*S*3]$^+$, calculated at B3LYP/SDD with PCM in dichloromethane (the Gaussian band shape with an exponential half-width, σ = 0.33 eV).

contributions of 72% for HOMO to LUMO transitions. Indeed, there are some other intense bands on the simulated spectra, which are also close to the experimental bands (Fig. 10, Table 2). The frontier molecular orbitals, HOMO and LUMO are shown in Fig. 15. The HOMO is only localized on the metal–d_{z^2} electron moiety, while the LUMO is localized on both the metal–d_{z^2} and ligand–π moieties. The energy gap between the HOMO and LUMO is considerably low (ΔE_g = 17.58 kcal mol^{-1}) and thus involves a significant contribution in the excitation protocol.

Excited state properties and Δ *vs.* Λ-chirality at-metal in solution

The four-coordinated and slightly distorted square-planar metal complexes with asymmetrical bidentate chiral ligands and with ligand folding angles (with respect to the coordination plane around the metal ion) explore induced chirality at-metal and afford mixtures of the two diastereomers (Δ and Λ), which diastereoselectively favours one as the major diastereomer (Fig. 9),[29b] as discussed above. Though the induced chirality and diastereoselection phenomena are quantitative in the solid-state (evidenced by using the X-ray and DSC analyses), a dynamic diastereomeric equilibrium between the two diastereomers prevails in solution (evidenced by using the variable time and temperature ^{1}H NMR, ECD and VCD spectra).[29–31] We

Table 2 Some selected and simplified assignments on the simulated spectrum for **Λ-[Pd(pic)*R*3]**$^+$, calculated at B3LYP/SDD with PCM in dichloromethane

λ/nm[a]	Oscillator strength (f)	MO contribution[b] (%)	Assignments[c]
405 (410sh)	0.0168	H−1 → L + 1 (67), H → L (25)	MM, ML
373 (390)	0.0513	H−1 → L + 1 (22), H → L (72)	MM, ML
285 (280sh)	0.2885	H−3 → L (26), H−2 → L (62)	MM, ML, LL
249 (255)	0.1092	H−4 → L + 2 (17), H → L + 7 (39)	MM, ML, LL
239	0.5760	H−6 → L (24), H → L + 7 (28)	MM, ML, LL

[a] The experimental values are in parentheses. [b] H/L for HOMO/LUMO. [c] MM, ML and LL for metal-centered (d–d), metal–ligand/ligand–metal and ligand-centered transitions, respectively.

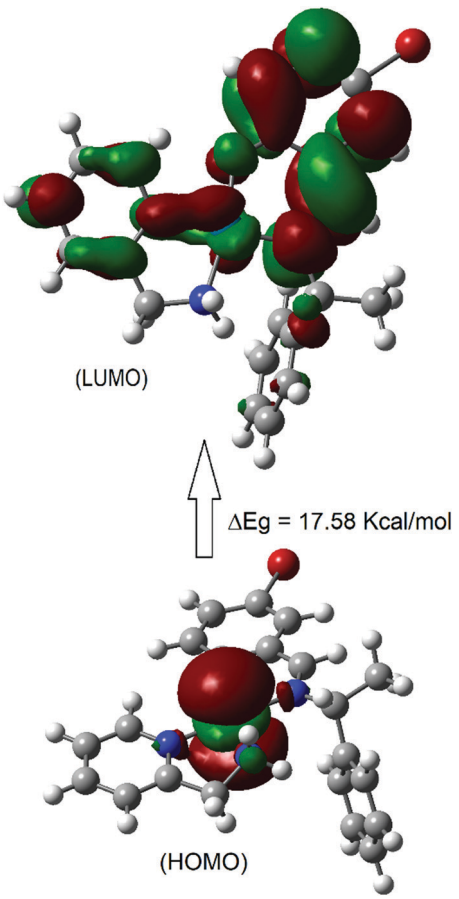

Fig. 15 The frontier molecular orbitals, HOMO and LUMO for **Λ-[Pd(pic)*R*3]**$^+$, calculated at B3LYP/SDD with PCM in dichloromethane.

attempted to correlate the experimental ECD spectra with the calculated spectra and hence to estimate the equilibrium shift (*i.e.*, the preferred formation of diastereomer) in solution. It is well documented that the overall nature of the chiral metal-complexes is mainly reflected by their ECD spectra, which, in particular, are used to determine the absolute configuration at the metal center (*i.e.*, Λ *vs.* Δ) following the MLCT and/or d–d transition bands in solution. In fact, combined studies on the experimental and calculated ECD spectra have successfully been used to determine the absolute configuration at-metal, resulting from induced chirality and diastereoselection in *S* or *R*-ligated complexes.[29–31] Thus, the comparison of the experimental ECD spectrum for **[Pd(pic)*R*3]NO$_3$** with the calculated spectra for the diastereomeric pair **Λ-[Pd(pic)*R*3]**$^+$**/Δ-[Pd(pic)*R*3]**$^+$ shows the experimental spectrum to correspond well to **Λ-[Pd(pic)*R*3]**$^+$ (Fig. 14). The results suggest that the spectrum for **[Pd(pic)*R*3]NO$_3$** corresponds to a diastereomeric excess of **Λ-[Pd(pic)*R*3]**$^+$ (*i.e.*, the major diastereomer) in solution. Similarly, the spectrum for **[Pd(pic)*S*3]NO$_3$** corresponds to a diastereomeric excess of **Δ-[Pd(pic)*S*3]**$^+$ (*i.e.*, the major diastereomer) in solution (Fig. 14). The ^{1}H NMR spectrum for **[Pd(pic)*R*3]NO$_3$** in $CDCl_3$ (Fig. 5) shows one set of peaks for each proton, in contrast to the expected two sets of peaks for each proton corresponding to the two diastereomers,[30a,b] suggesting a rapid dynamic diastereomeric equilibrium between the two diastereomers in the context of the ^{1}H NMR time scale in solution.

Biological evaluation of the compounds

Stability. All compounds were evaluated over time by monitoring their stability in DMSO, the co-solvent used for the biological assays. These studies were performed during 24 h at room temperature by using ^{1}H NMR in DMSO-d_6.

From the X-ray studies of the **[Pd(pic)*R*3]NO$_3$** and **[Pd(pic)*rac*2]NO$_3$** complexes, we proved that only isomer **A** can be formed for the Pd(II)-complexes (Fig. 8). Also, a certain configuration at the ligand, *R* or *S*, causes a quantitative induction of a certain configuration at the metal ions (diastereoselection) as Λ for the **[Pd(pic)*R*]NO$_3$** and Δ for **[Pd(pic)*S*]NO$_3$** complexes. The appearance of two signals in DMSO-d_6, different from the solid state and deuterated chloroform solution, clearly indicates the existence of an equilibrium between Δ- and Λ-diastereomers for all the Pd(II)-complexes except **[Pd(pic)*R*5]NO$_3$** (not detectable) (for example see the ^{1}H NMR spectra of **[Pd(pic)*S*2]NO$_3$** and **[Pd(pic)*R*5]NO$_3$** in Fig. S10, ESI†). As shown in Fig. 16 and Fig. S10 (ESI†), we can see only one peak for the methyl proton in **[Pd(pic)*R*5]NO$_3$**. Also, in all complexes except **[Pd(pic)*S*1]NO$_3$**, the equilibrium is towards the stable diastereomer (Λ-diastereomer for the **[Pd(pic)*R*]NO$_3$** complexes and Δ-diastereomer for the **[Pd(pic)*S*]NO$_3$** complexes) (Table 3).

For a quantitative evaluation, we chose the methyl proton represented by a doublet above 1.5 ppm for each diastereomer (Fig. 16). In accordance with the X-ray structures in the solid-state of **[Pd(pic)*R*3]NO$_3$** and **[Pd(pic)*rac*2]NO$_3$**, we assume that the methyl proton peak with a higher integration value relatively downfield corresponds to the major diastereomer

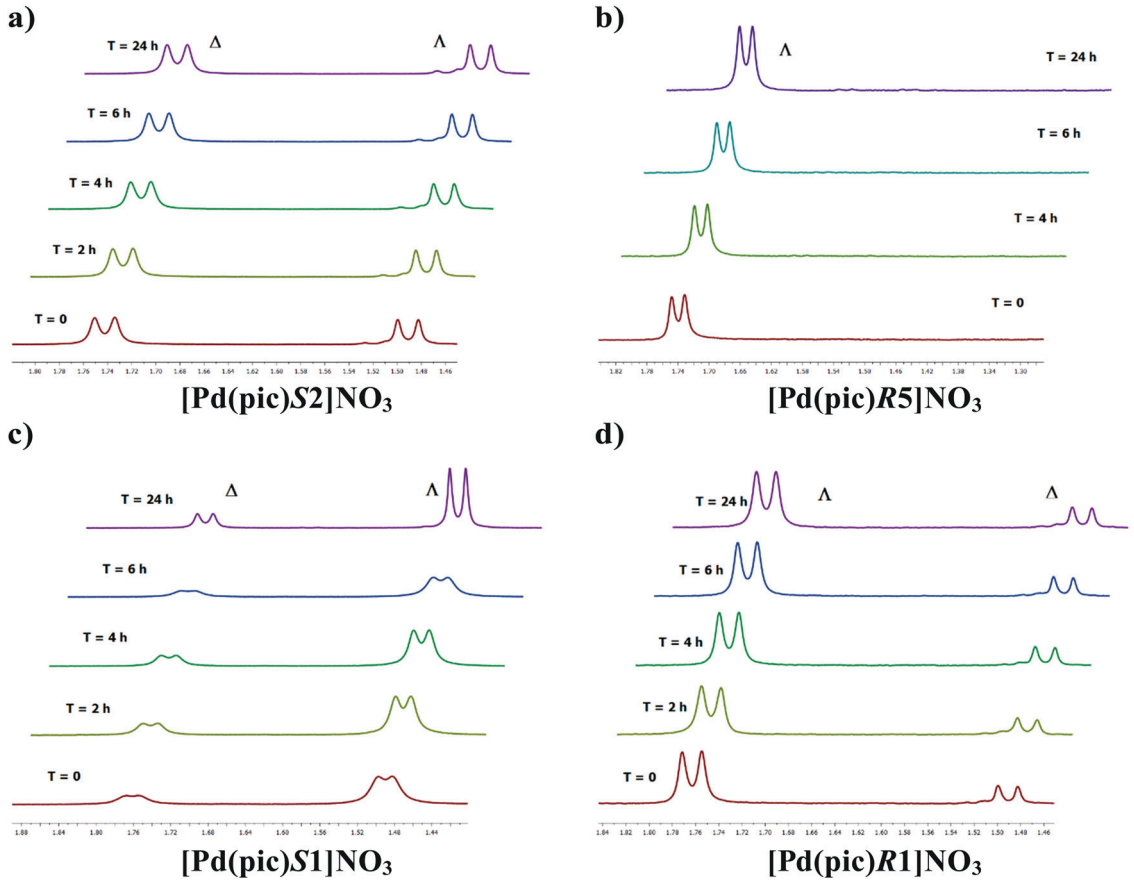

Fig. 16 Display of part of the VT ^{1}H NMR spectrum of **[Pd(pic)*S*2]NO$_3$**, **[Pd(pic)*R*5]NO$_3$**, **[Pd(pic)*S*1]NO$_3$** and **[Pd(pic)*R*1]NO$_3$** in DMSO-d_6 solution. The NMR signals around 1.75 ppm and 1.50 ppm account for the methyl proton of the Δ- and Λ-diastereomers.

Table 3 Change of diastereomers in Λ- or Δ-Pd-*R* (Δ- or Λ-Pd-*S*) at variable times recorded by ^{1}H NMR in DMSO-d_6. The diastereomeric ratio (%) is from the integration of the methyl proton signals

	%	
Compound	Λ/Δ (in initial time)	Λ/Δ (after 24 h)
[Pd(pic)*R*1]NO$_3$	78/22	78/22
[Pd(pic)*R*2]NO$_3$	72/28	71/29
[Pd(pic)*R*3]NO$_3$	77.5/22.5	77.5/22.5
[Pd(pic)*R*4]NO$_3$	86/14	84/16
[Pd(pic)*R*5]NO$_3$	100/0	100/0
[Pd(pic)*R*6]NO$_3$	78/22	78/22
[Pd(pic)*R*7]NO$_3$	78/22	78/22
[Pd(pic)*S*1]NO$_3$	74/26	74/26
[Pd(pic)*S*2]NO$_3$	40/60	41/59
[Pd(pic)*S*3]NO$_3$	19/81	19/81
[Pd(pic)*S*$_4$]NO$_3$	10/90	10/90
[Pd(pic)*S*5]NO$_3$	7.5/92.5	5.5/94.5
[Pd(pic)*S*6]NO$_3$	23/77	22/78
[Pd(pic)*S*7]NO$_3$	34/66	34/66

(Λ for (**[Pd(pic)*R*]NO$_3$** and Δ for (**[Pd(pic)*S*]NO$_3$**) and the downfield one to the minor diastereomer (Δ for (**[Pd(pic)*R*]NO$_3$** and Λ for (**[Pd(pic)*S*]NO$_3$**) in solution (Fig. 16). We estimated the ratios of diastereomers (Λ:Δ in %) based on the integration values of the methyl proton peaks at *ca.* δ 1.75 and 1.50 ppm (Table 3). The variation in diastereomeric ratios suggests a unique equilibrium between the Λ- and Δ-diastereomers for each complex in solution, which is obviously different for different substituents on the salicylaldehyde ring. This suggests that the substitution at the salicylaldehyde ring has a strong impact on the thermodynamic equilibrium.

Also, the ratio of the diastereomers remains unaltered (or with small changes) during the whole experimental time (Table 3). This result indicates that the kinetics for the Λ- to Δ- interconversions do not depend on the substituents on the salicylaldehyde ring.

All compounds are stable in this solvent (DMSO-d_6). The only exception was observed for the compound **[Pd(pic)*S*1]NO$_3$**, in which the precipitation of a blackish product was observed, while the compound remaining in solution maintained its original structure.

According to the VT ^{1}H NMR data, the equilibrium for both the **[Pd(pic)*S*1]NO$_3$** and **[Pd(pic)*R*1]NO$_3$** complexes is towards the Λ-diastereomer (Fig. 16 and Table 3). These results are in agreement with the other results for **[Pd(pic)*R*1]NO$_3$** and in contradiction with the other results for **[Pd(pic)*S*1]NO$_3$**. It should be noted that the **[Pd(pic)*R*1]NO$_3$** and **[Pd(pic)*S*1]NO$_3$** complexes are the only complexes without halogen-substituted on the salicylaldehyde ring.

Cytotoxicity assessment of the Pd(II)-complexes in MDA-MB-231 and MCF-7 breast cancer cell lines

The cytotoxic activity of all fourteen complexes was tested in the human breast cancer cell lines MDA-MB-231 and MCF-7 at 24 h, using the colorimetric MTT assay. These cell lines were chosen considering their different degrees of aggressiveness. While MDA-MB-231 is hormone independent and invasive, being highly aggressive, MCF-7 is hormone dependent and non-invasive. The cells were treated with the compounds within the concentration range of 0.1 μM to 100 μM. All compounds are cytotoxic in the conditions tested with the IC_{50} values ranging from 5.8 to 45.5 μM in MDA-MB-231 cells and 5.5 to 21.7 μM in MCF-7 cells (Table 4), thus being more active in the hormone dependent cell lines. Importantly, the introduction of the halogen(s) at the Schiff base led to an increase of cytotoxicity up to ~6 and 8-fold for *R* and *S* isomers, respectively, in the MDA-MB-231 cell line, and up to ~3 and 4-fold for *R* and *S* isomers, respectively, in the MCF-7 cell line. Also, the double functionalization afforded more cytotoxic compounds, evidencing the role of halogen in the overall activity (Fig. 17). Compounds with two iodine substituents, **[Pd(pic)*R*6]NO_3** and **[Pd(pic)*S*6]NO_3**, exhibited the highest cytotoxicity. Compared with the data from the literature, one can observe that some of the Pd(II)-complexes presented here are among the best reported in the MDA-MB-231 cell line (taking also into consideration the incubation time)[38] and also much better than cisplatin in the same experimental conditions (122 ± 25 μM).[39] Kumar *et al.* described a series of palladium complexes of the 1,2,4-triazole-derived chiral N-heterocyclic carbene ligands aiming at studying the influence of chirality on the compound's anticancer activity.[16a] The authors did not see any chirality-related influence for any of the enantiomeric pairs, an outcome that is in agreement with what we observed with our Pd(II)-complexes endowed with chiral Schiff bases.

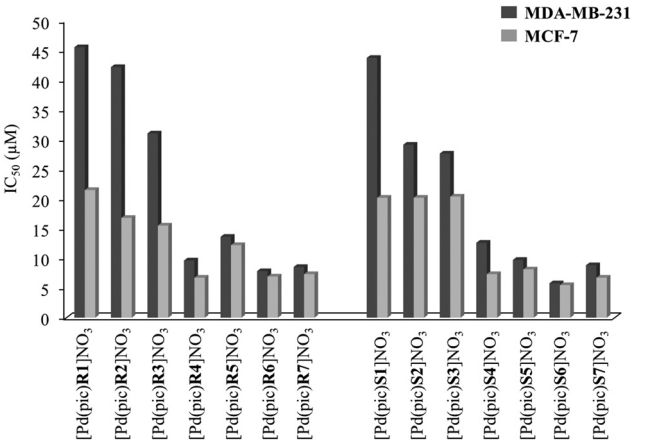

Fig. 17 IC_{50} values (μM) obtained at 24 h incubation for the enantiomeric pairs in the MDA-MB-231 and MCF-7 breast cancer cells.

The effects of the Pd(II)-complexes in the colony formation potential of the MDA-MB-231 cells

To evaluate the colony formation potential of the Pd(II)-complexes, the MDA-MB-231 breast cancer derived cell line was exposed to 1/4 of the IC_{50} values and the IC_{50} values of the different compounds for 24 hours, after which the cellular medium was removed and the cells were maintained in the culture for 8 days, mimicking what would happen in a chemotherapy cycle. Our results showed that all tested compounds significantly reduce the ability of the cells to form colonies at the IC_{50} values (Fig. S11, ESI†). When the concentration was decreased to 25% of the IC_{50} values, the differences between the compounds could be noticed (Fig. 18). In this case, it seems that the majority of the *R* enantiomers are more efficient in inhibiting the colony formation ability of the MDA-MB-231 cells than their *S* pairs. This could possibly indicate differences in the mechanism of action of the different enantiomers. It is also important to mention that the ability of the compounds to inhibit the formation of colonies does not correlate with their cytotoxicity. For example, the compound **[Pd(pic)*S*7]NO_3** is the most cytotoxic compound; yet it is the compound where at 1/4 of the IC_{50} values, more colonies are detected. In contrast, **[Pd(pic)*R*1]NO_3** was the compound with the highest IC_{50}, but it showed remarkable ability to inhibit the formation of colonies.

Evaluation of the cell death mechanism induced by selected compounds

The cell death mechanism was assessed using the annexin V/propidium iodide (AV/PI) cytometry-based assay. Annexin V is a marker of early apoptosis, while PI is a marker of necrosis. For this assay, three pairs of compounds were selected, **[Pd(pic)*R*6]NO_3/[Pd(pic)*S*6]NO_3** and **[Pd(pic)*R*7]NO_3/[Pd(pic)*S*7]NO_3** given the good cytotoxicity presented by these compounds, and **[Pd(pic)*R*2]NO_3/[Pd(pic)*S*2]NO_3**, since these pairs of isomers were very efficient in inhibiting the formation of the MDA-MB-231 cell colonies. Thus, the cancer cells were

Table 4 IC_{50} values (μM) for the Pd(II)-complexes at 24 h incubation, in MDA-MB-231 and MCF-7 breast cancer cells

	IC_{50}			IC_{50}	
Compound	MDA-MB-231	MCF-7	Compound	MDA-MB-231	MCF-7
[Pd(pic)*R*1]NO_3	45.5 ± 5.3	21.5 ± 1.1	**[Pd(pic)*S*1]NO_3**	43.7 ± 10.0	20.2 ± 1.3
[Pd(pic)*R*2]NO_3	42.2 ± 2.7	16.8 ± 1.2	**[Pd(pic)*S*2]NO_3**	29.1 ± 2.0	20.2 ± 1.1
[Pd(pic)*R*3]NO_3	31.0 ± 2.2	15.5 ± 0.9	**[Pd(pic)*S*3]NO_3**	27.6 ± 2.3	20.4 ± 1.5
[Pd(pic)*R*4]NO_3	9.6 ± 1.2	6.7 ± 0.8	**[Pd(pic)*S*4]NO_3**	12.6 ± 0.8	7.3 ± 0.4
[Pd(pic)*R*5]NO_3	13.6 ± 0.9	12.2 ± 0.6	**[Pd(pic)*S*5]NO_3**	9.7 ± 0.7	8.1 ± 0.9
[Pd(pic)*R*6]NO_3	7.8 ± 0.5	6.9 ± 0.3	**[Pd(pic)*S*6]NO_3**	5.8 ± 0.4	5.5 ± 0.4
[Pd(pic)*R*7]NO_3	8.5 ± 0.7	7.3 ± 0.4	**[Pd(pic)*S*7]NO_3**	8.8 ± 0.8	6.7 ± 0.4

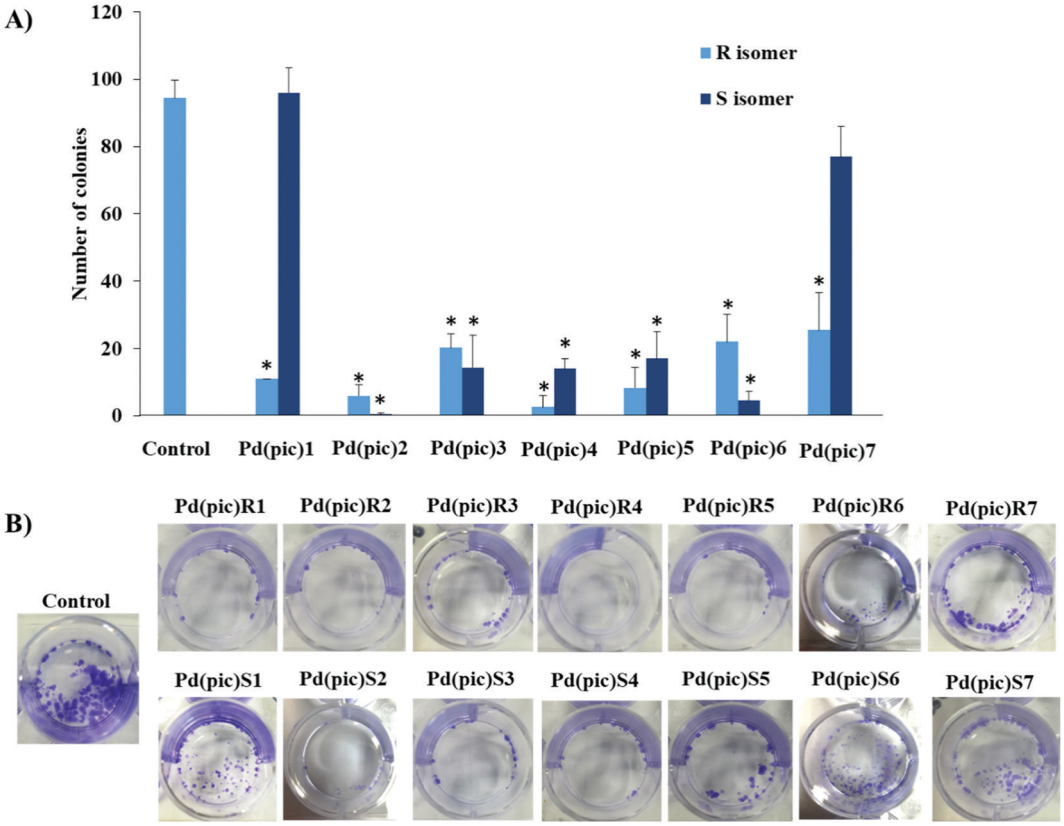

Fig. 18 Colony formation assay of the MDA-MB-231 cell line after exposure to the Pd(II)-complexes. (A) The analysis of the clonogenic ability, after 24 h of incubation with 1/4 of the IC_{50} values. The values represent mean ± S.D. of at least two independent experiments. Statistical analysis was performed by one-way ANOVA with Dunnett's multiple comparisons test. *$P \leq 0.0001$ compared with control. (B) The representative images of the colony formation assay in the MDA-MB-231 cell line.

Table 5 Percentage of MDA-MB-231 cells in each state after treatment with complexes **[Pd(pic)*R*2]NO_3**, **[Pd(pic)*S*2]NO_3**, **[Pd(pic)*R*6]NO_3**, **[Pd(pic)*S*6]NO_3**, **[Pd(pic)*R*7]NO_3** and **[Pd(pic)*S*7]NO_3** at IC_{50} concentrations for 24 h incubation

	% Vital cells AV^-/PI^-	% Apoptotic cells AV^+/PI^-	% Late apoptotic cells AV^+/PI^+	% Necrosis AV^-/PI^+
Control	99.6	0.1	0.2	0.1
[Pd(pic)*R*2]NO_3	41.5	19.4	36.4	2.7
[Pd(pic)*S*2]NO_3	70.0	19.7	7.7	2.6
[Pd(pic)*R*6]NO_3	31.9	29.9	32.8	5.4
[Pd(pic)*S*6]NO_3	59.4	21.7	15.4	3.5
[Pd(pic)*R*7]NO_3	66.7	18.6	11.2	3.5
[Pd(pic)*S*7]NO_3	64.5	19.5	12.2	3.8

incubated with the compounds for 24 h at their IC_{50} values. The results show that all compounds led to an increase in the percentage of the AV^+/PI^- and AV^+/PI^+ stained cells (Table 5) in comparison to the negative control indicating that they induce cell death by apoptosis.

Conclusions

A series of heteroleptic enantiopure [Pd(pic)(*R* or *S*)-*N*-1-(phenyl)ethyl-2,4-X_1,X_2-salicylaldiminate)]NO_3, [Pd(pic)(*R* or *S*)]NO_3 complexes were synthesized from the reaction between $[Pd(pic)Cl_2]$ (pic = 2-picolylamine) and the enantiopure Schiff bases (*R* or *S*)-*N*-1-(phenyl)ethyl-2,4-X_1,X_2-salicylaldimine. The single crystal X-ray structural analyses revealed that the compounds have pseudo square-planar geometry around the metal center. The observed mirror–image relationships of the ECD spectra suggest enantiomeric excess of the [Pd(pic)*R*]NO_3 and [Pd(pic)*S*]NO_3 in solution. The combined studies on the X-ray structures, ECD spectra and DFT/TDDFT calculations explore the induced chirality at the metal center, which diastereoselectively prefers Λ-$[Pd(pic)R3]^+$ as the major diastereomer in the solid-state,

gas phase or solution. The anticancer activity of all compounds was assessed against MDA-MB-231 and MCF-7 cancer cells and showed that all Pd(II)-complexes are cytotoxic in the conditions they were tested. The introduction of halogens to the Schiff base ligands led to a clear increase of cytotoxicity. Moreover, all compounds inhibited the formation of MDA-MB-231 colonies to different extents and induced cell death by apoptosis, indicating in some cases the involvement of chirality-related mechanisms. Further studies to elucidate the active species are presently underway.

Experimental section

Chemicals and instrumentation

$PdCl_2$, $AgNO_3$, 5-bromosalicylaldehyde, 5-chlorosalicyladehyde, 3,5-dibromosalicylaldehyde, 3,5-diiodosalicylaldehyde, 3,5-dichlorosalicylaldehyde, 3-bromo-5-chlorosalicylaldehyde, salicylaldehyde, 2-picolylamine, (*R*)-(+)-α-methylbenzylamine and (*S*)-(−)-α-methylbenzylamine were purchased from Sigma-Aldrich and used without further purification. Commercial solvents were distilled and then used for the preparation of the ligands and complexes. The FT-IR spectra were recorded on a JASCO, FT/IR-6300 spectrometer (4000–400 cm^{-1}) in KBr pellets. The ^1H and ^{13}C NMR spectra were recorded on a Bruker Avance III 400 spectrometer at room temperature. The elemental analyses were performed on Leco, CHNS-932 and PerkinElmer 7300 DV elemental analyzers. The electronic absorption spectra (UV–vis) were recorded with a PerkinElmer Lambda 35 spectrophotometer. The electronic circular dichroism (ECD) spectra were recorded at *ca.* 25 °C on a Jasco J-720 spectropolarimeter with a UV–vis (180–800 nm) photomultiplier (EXEL-308). The stock solutions of the complexes were prepared in CH_2Cl_2 at *ca.* 2.0 mM. Dilutions were made to measure the spectra at different concentrations, typically 20–85 μM and 200 μM. The ECD measurements were done using quartz Suprasil® cells of 0.2 or 1.0 cm optical path. The ΔA values measured correspond to $\Delta A = \Delta\varepsilon \times b \times C$, where b is the optical path and C is the concentration of the complex. The measuring conditions were as follows: data pitch of 0.5 nm, speed of 200 nm min^{-1}, response of 2 s, bandwidth of 0.5 nm, and 3 accumulations.

Synthesis of the chiral Schiff bases

All chiral Schiff base ligands were synthesized using identical reaction conditions and were achieved by the Schiff condensation of (*R*)-(+)-α-methylbenzylamine and (*S*)-(−)-α-methylbenzylamine with the appropriate halogen substituted salicylaldehyde in aqueous solution as previously published.[23]

H*R*1. Yield: 90%. Analysis calculated for $C_{15}H_{15}NO$ (225.29): C, 79.97; H, 6.71; and N, 6.22. Found: C, 80.06; H, 6.52; and N, 6.25%. The ^1H-NMR data [400 MHz, $CDCl_3$] δ (ppm): 13.60 [s, 1H (OH)]; 8.44 [s, 1H (imine)]; 7.39–6.88 [m, 9H (Ar)]; 4.58 [q, 1H (benzyl)]; and 1.66 [d, 3H (methyl)]. The ^{13}C-NMR data [100 MHz, $CDCl_3$, in ppm]: 162.9 (C═N), 160.5, 143.3, 131.8, 130.9, 128.2, 128.8, 125.9, 118.3, 118.1, 68.0 (chiral C), and 24.5 (CH_3). The IR data (KBr, cm^{-1}): 3433m (br, νOH), 3062, 2924w (νC–H) and 1628vs (νC═N).

H*R*2. Yield: 93%. Analysis calculated for $C_{15}H_{14}ClNO$ (259.73): C, 69.37; H, 5.43; and N, 5.39. Found: C, 69.28; H, 5.50; and N, 5.67%. The ^1H-NMR data [400 MHz, $CDCl_3$] δ (ppm): 13.54 [s, 1H (OH)]; 8.36 [s, 1H (imine)]; 7.56–6.93 [m, 8H (Ar)]; 4.61 [q, 1H (benzyl)]; and 1.66 [d, 3H (methyl)]. The ^{13}C-NMR data [100 MHz, $CDCl_3$, in ppm]: 162.2 (C═N), 160.1, 143.3, 136.9, 132.5, 128.7, 126.5, 119.4, 68.4 (chiral C), and 24.8 (CH_3). The IR data (KBr, cm^{-1}): 3434m (br, νOH), 2928w (νC–H) and 1630vs (νC═N).

H*R*3. Yield: 97%. Analysis calculated for $C_{15}H_{14}BrNO$ (303.05): C, 59.23; H, 4.64; and N, 4.60. Found: C, 59.89; H, 4.58; and N, 6.39%. The ^1H-NMR data [400 MHz, $CDCl_3$] δ (ppm): 13.60 [s, 1H (OH)]; 8.34 [s, 1H (imine)]; 7.41–6.87 [m, 8H (Ar)]; 4.60 [q, 1H (benzyl)]; and 1.66 [d, 3H (methyl)]. The ^{13}C-NMR data [100 MHz, $CDCl_3$, in ppm]: 162.2 (C═N), 160.0, 143.3, 134.9, 133.9, 127.8, 127.4, 126.4, 120.2, 119.0, 68.4 (chiral C), and 24.7 (CH_3). The IR data (KBr, cm^{-1}): 3429m (br, νOH), 2919w (νC–H) and 1625vs (νC═N).

The other ligands were fully characterized in a previous article.[23]

Synthesis of the complexes

[Pd(pic)Cl_2] was synthesized and purified as previously described.[33] The synthesis of all complexes followed a generic synthetic route. Briefly, to a stirring aqueous solution of 1 mmol of [Pd(pic)Cl_2], 2 mmol of $AgNO_3$ was added at 20 °C in the dark. After the white AgCl precipitate was filtered off, 1 mmol of the appropriate ligand dissolved in methanol was added to the yellow filtrate and the solution was refluxed for 2 h. After reducing the volume of the solvent, the yellow precipitate was formed. The precipitate was collected by filtration, washed with cold methanol and diethyl ether and dried in air.

R and *S*-enantiomers have identical IR- and NMR-spectra.

[Pd(pic)*S*1]NO_3 and [Pd(pic)*R*1]NO_3

Yield: 81% and 87%, respectively. Analysis calculated for $C_{21}H_{22}N_4O_4Pd$: C, 50.36; H, 4.43; and N, 11.19. Found for [Pd(pic)*S*-1]NO_3: C, 50.39; H, 4.41; and N, 11.23%. Found for [Pd(pic)*R*-1]NO_3: C, 50.40; H, 4.45; and N, 11.21%. The ^1H-NMR data [400 MHz, $CDCl_3$] δ (ppm): 8.65 [d, 1H (imine)]; 7.78–6.62 [m, 13H (Ar)]; 5.94, 4.08 [m, 2H (NH_2)]; 5.36 [q, 1H (benzyl)]; and 4.35, 4.14 [t of d, 2H (CH_2)], 1.77 [d, 3H (CH_3)]. The ^{13}C-NMR data [100 MHz, $CDCl_3$, in ppm]: 163.7 (C═N), 163.0, 160.9, 146.1, 141.7, 140.0, 136.2, 135.0, 129.5, 128.3, 126.8, 123.3, 121.3, 120.2, 119.6, 116.4, 68.3 (chiral C), 51.5, and 23.1 (CH_3). The IR data (KBr, cm^{-1}): 1612vs (νC═N), 1383vs (νNO_3), and 824vs (νNO_3).

[Pd(pic)*S*2]NO_3 and [Pd(pic)*R*2]NO_3. Yield: 92% and 86%, respectively. Analysis calculated for $C_{21}H_{21}ClN_4O_4Pd$: C, 47.12; H, 3.95; and N, 10.47. Found for [Pd(pic)*S*-2]NO_3: C, 47.07; H, 3.99; and N, 10.51%. Found for [Pd(pic)*R*-2]NO_3: C, 47.09; H, 3.94; and N, 10.43%. The ^1H-NMR data [400 MHz, $CDCl_3$] δ (ppm): 8.56 [d, 1H (imine)]; 7.76–6.89 [m, 12H (Ar)]; 5.92, 4.37 [m, 2H (NH_2)]; 5.21 [q, 1H (benzyl)]; and 4.18, 3.98 [t of d, 2H

(CH_2)], 1.67 [d, 3H (CH_3)]. The ^{13}C-NMR data [100 MHz, $CDCl_3$, in ppm]: 162.2 (C═N), 160.2, 143.3, 137.0, 132.5, 132.0, 130.5, 128.8, 127.4, 126.4, 119.4, 68.5 (chiral C), and 24.8 (CH_3). The IR data (KBr, cm^{-1}): 1615vs (νC═N), 1384vs (νNO_3), and 825vs (νNO_3).

[Pd(pic)*S*3]NO_3 and [Pd(pic)*R*3]NO_3. Yield: 85% and 90%, respectively. Analysis calculated for $C_{21}H_{21}BrN_4O_4Pd$: C, 43.51; H, 3.65; and N, 9.66. Found for [Pd(pic)*S*-3]NO_3: C, 43.51; H, 3.66; and N, 9.64%. Found for [Pd(pic)*R*-3]NO_3: C, 43.55; H, 3.61; and N, 8.69%. The ^{1}H-NMR data [400 MHz, $CDCl_3$] δ (ppm): 8.52 [d, 1H (imine)]; 7.75–6.79 [m, 12H (Ar)]; 6.01, 4.55 [m, 2H (NH_2)]; 5.17 [q, 1H (benzyl)]; and 4.18, 3.99 [t of d, 2H (CH_2)], 1.64 [d, 3H (CH_3)]. The ^{13}C-NMR data [100 MHz, $CDCl_3$, in ppm]: 162.2 (C═N), 162.2, 160.1, 143.4, 139.7, 135.6, 134.9, 133.5, 128.8, 127.4, 126.4, 120.2, 119.0, 68.4 (chiral C), and 24.7 (CH_3). The IR data (KBr, cm^{-1}): 1614vs (νC═N), 1384vs (νNO_3), and 822vs (νNO_3).

[Pd(pic)*S*4]NO_3 and [Pd(pic)*R*4]NO_3. Yield: 78% and 85%, respectively. Analysis calculated for $C_{21}H_{20}Cl_2N_4O_4Pd$: C, 44.27; H, 3.54; and N, 9.83. Found for [Pd(pic)*S*-4]NO_3: C, 44.24; H, 3.57; and N, 9.86%. Found for [Pd(pic)*R*-4]NO_3: C, 44.24; H, 3.53; and N, 9.81%. The ^{1}H-NMR data [400 MHz, $CDCl_3$] δ (ppm): 8.71 [d, 1H (imine)]; 7.66–6.96 [m, 11H (Ar)]; 5.79, 4.28 [m, 2H (NH_2)]; 5.10 [q, 1H (benzyl)]; and 4.08, 3.84 [t of d, 2H (CH_2)], 1.53 [d, 3H (CH_3)]. The ^{13}C-NMR data [100 MHz, $CDCl_3$, in ppm]: 162.2 (C═N), 160.1, 143.4, 139.7, 135.6, 134.9, 133.5, 128.8, 127.4, 126.4, 123.6, 119.8, 68.8 (chiral C), and 23.1 (CH_3). The IR data (KBr, cm^{-1}): 1620vs (νC═N), 1383vs (νNO_3), and 820vs (νNO_3).

[Pd(pic)*S*5]NO_3 and [Pd(pic)*R*5]NO_3. Yield: 86% and 91%, respectively. Analysis calculated for $C_{21}H_{20}Br_2N_4O_4Pd$: C, 38.30; H, 3.06; and N, 8.51. Found for [Pd(pic)*S*-5]NO_3: C, 38.32; H, 3.11; and N, 8.54%. Found for [Pd(pic)*R*-5]NO_3: C, 38.34; H, 3.10; and N, 8.55%. The ^{1}H-NMR data [400 MHz, $CDCl_3$] δ (ppm): 9.05 [d, 1H (imine)]; 7.92–7.34 [m, 11H (Ar)]; 6.34, 4.65 [m, 2H (NH_2)]; 5.36 [q, 1H (benzyl)]; and 4.35, 4.13 [t of d, 2H (CH_2)], 1.77 [d, 3H (CH_3)]. The ^{13}C-NMR data [100 MHz, $CDCl_3$, in ppm]: 163.8 (C═N), 160.7, 147.1, 142.0, 136.0, 134.9, 129.6, 128.6, 127.0, 123.5, 121.8, 121.2, 115.2, 68.7 (chiral C), and 23.0 (CH_3). The IR data (KBr, cm^{-1}): 1612vs (νC═N), 1384vs (νNO_3), and 860vs (νNO_3).

[Pd(pic)*S*6]NO_3 and [Pd(pic)*R*6]NO_3. Yield: 81% and 90%, respectively. Analysis calculated for $C_{21}H_{20}I_2N_4O_4Pd$: C, 33.51; H, 2.68; and N, 7.44. Found for [Pd(pic)*S*-6]NO_3: C, 33.48; H, 2.69; and N, 7.40%.; Found for [Pd(pic)*R*-6]NO_3: C, 33.50; H, 2.67; and N, 7.44%. The ^{1}H-NMR data [400 MHz, $CDCl_3$] δ (ppm): 9.14 [d, 1H (imine)]; 8.04–7.27 [m, 11H (Ar)]; 6.10, 4.51 [m, 2H (NH_2)]; 5.22 [q, 1H (benzyl)]; and 4.20, 4.00 [t of d, 2H (CH_2)], 1.66 [d, 3H (CH_3)]. The ^{13}C-NMR data [100 MHz, $CDCl_3$, in ppm]: 163.7 (C═N), 160.4, 151.5, 147.9, 143.7, 140.2, 138.0, 129.5, 128.6, 127.1, 123.3, 121.3, 115.2, 68.5 (chiral C), and 22.8 (CH_3). The IR data (KBr, cm^{-1}): 1612vs (νC═N), 1384vs (νNO_3), 825vs (νNO_3).

[Pd(pic)*S*7]NO_3 and [Pd(pic)*R*7]NO_3. Yield: 79% and 87%, respectively. Analysis calculated for $C_{21}H_{20}BrClN_4O_4Pd$: C, 41.07; H, 3.28; and N, 9.12. Found for [Pd(pic)*S*-7]NO_3: C, 41.05; H, 3.24; and N, 9.11%. Found for [Pd(pic)*R*-7]NO_3: C, 41.05; H, 3.32; and N, 9.10%. The ^{1}H-NMR data [400 MHz, $CDCl_3$] δ (ppm): 9.07 [d, 1H (imine)]; 7.90–7.24 [m, 11H (Ar)]; 6.22, 4.42 [m, 2H (NH_2)]; 5.36 [q, 1H (benzyl)]; and 4.32, 4.09 [t of d, 2H (CH_2)], 1.78 [d, 3H (CH_3)]. The ^{13}C-NMR data [100 MHz, $CDCl_3$, in ppm]: 163.1 (C═N), 160.5, 147.1, 140.2, 138.1, 132.9, 129.6, 128.6, 127.0, 123.5, 121.3, 117.2, 68.7 (chiral C), and 23.0 (CH_3). The IR data (KBr, cm^{-1}): 1614vs (νC═N), 1383vs (νNO_3), 834vs (νNO_3).

[Pd(pic)rac2]NO_3. This complex was prepared exclusively for the purpose of growing X-ray-quality crystals and theoretical calculations. Its ^{1}H NMR spectra were identical with those of **[Pd(pic)*R*2]NO_3** and **[Pd(pic)*S*2]NO_3**. The yield is more than 85%. Other analytical data were not determined. The route for the synthesis of this compound is similar to other complexes. The only difference is the use of the racemic Schiff base ligand, (*R*/*S*)-*N*-1-(phenyl)ethyl-2,4-Cl-salicylaldimine, instead of the enantiopure Schiff base ligand, (*R* or *S*)-*N*-1-(phenyl)ethyl-2,4-Cl-salicylaldimine.

Single crystal X-ray details

The X-ray crystal data for **[Pd(pic)*R*3]NO_3** were collected from multi-faceted crystals of suitable size and quality selected from a representative sample of crystals of the same habit using an optical microscope. In each case, the crystals were mounted on MiTiGen loops, and the data collection was carried out in a cold stream of nitrogen (150(2) K; Bruker D8 QUEST ECO; Mo K_α radiation). All diffractometer manipulations were carried out using the Bruker APEX3 software.[40] The structure solution and refinement were carried out using the XS, XT and XL software, embedded within the Bruker SHELXTL suite.[41] For each structure, the absence of additional symmetry was confirmed using ADDSYM incorporated in the PLATON program.[42]

The single-crystal X-ray diffraction data for **[Pd(pic)*rac*2]NO_3** were collected using an Oxford Diffraction Gemini R Ultra diffractometer (Cu K_α, multilayer mirror, Ruby CCD area detector) at 295(2) K. Data collection, unit cell determination and data reduction were carried out using the CrysAlis PRO software package[43] using the Olex2[44] interface. The structure was solved with the SHELXT 2015[45] structure solution program by intrinsic phasing methods and refined by full-matrix least squares on $|F|^2$ using SHELXL-2018/3.[45] The non-hydrogen atoms were refined anisotropically.

More details concerning both crystal structures and their refinements can be found in Table 6 or in the corresponding CIF files (ESI).

Computational method

To rationalize the experimental results, a computational procedure was performed with Gaussian 09.[46] For optimization in the gas phase, the initial geometry of the complex was generated from the X-ray structure of **[Pd(pic)*R*3]NO_3**. The four-coordinated and slightly distorted square-planar metal(II)-complexes with asymmetric bidentate chiral-Schiff base ligands

Table 6 Crystallographic data for [Pd(pic)*R*3]NO_3 and [Pd(pic)*rac*2]NO_3

	[Pd(pic)*R*3]NO_3	[Pd(pic)*rac*2]NO_3
Empirical formula	$C_{21}H_{21}BrN_4O_4Pd$	$C_{21}H_{21}ClN_4O_4Pd$
Formula weight	579.73	535.27
Temperature (K)	150(2)	295(2)
Wavelength (Å)	0.71073	1.54184
Crystal system	Orthorhombic	Triclinic
Space group	$P2_12_12_1$	$P\bar{1}$
a (Å)	7.0780(3)	9.0681(3)
b (Å)	14.5585(5)	10.7643(3)
c (Å)	20.1360(8)	11.5628(4)
α (°)		90.106(3)
β (°)		109.775(3)
γ (°)		93.914(3)
Volume (Å^3)	2074.92(14)	1059.25(6)
Z/calculated density (g cm^{-3})	4/1.856	2/1.678
Absorption coefficient (mm^{-1})	2.858	8.544
F(000)	1152	540
θ range (°)	2.460 to 33.193	4.118 to 67.003
h; k; l ranges	±10; ±22; −31, 30	±10; ±12; −12, 13
Reflections collected/unique	47 690/7903 $R_{(int)}$ = 0.0457]	8646/3732 [$R_{(int)}$ = 0.0285]
Refinement method	Full-matrix least-squares on F^2	Full-matrix least-squares on F^2
Data/restraints/parameters	7903/0/312	3732/0/289
Goodness-of-fit on F^2	1.043	1.048
Final R indices [$I > 2\sigma(I)$]	R_1 = 0.0279/wR_2 = 0.05	R_1 = 0.0271/wR_2 = 0.0691
R indices (all data)	R_1 = 0.0377/wR_2 = 0.0533	R_1 = 0.0284/wR_2 = 0.0704
Absolute structure parameter	0.034(8)	
Largest difference peak and hole (e Å^{-3})	0.763 and −0.675	0.569 and −0.441
CCDC number	1989598	2007895

and with ligand folding angles (*i.e.*, angles between the co-ordination plane around metal ion and the phenyl- and salicylal-rings) exhibit induced chirality at-metal and provide two diastereomers with opposite configurations (*i.e.*, Δ-Pd and Λ-Pd) along the C_2-symmetry of the molecule.[29b] Thus, based on the X-ray structure (dihedral angles and ligand folding angles), **[Pd(pic)*R*3]$^+$** can be best described as a Λ-diastereomer (*i.e.*, **Λ-[Pd(pic)*R*3]$^+$**). Therefore, the geometry of the opposite configured diastereomer **Δ-[Pd(pic)*R*3]$^+$** was built by mirror inversion of **Λ-[Pd(pic)*R*3]$^+$**, followed by manual inversion of the chiral-carbon center.[29–31] The DFT optimizations for the diastereomeric pair **Λ-[Pd(pic)*R*3]$^+$/Δ-[Pd(pic)*R*3]$^+$** and the enantiomeric pair **Λ-[Pd(pic)*R*3]$^+$/Λ-[Pd(pic)*S*3]$^+$** were carried out using the functional B3LYP and the basis sets SDD and LANL2DZ, respectively (Fig. 9 and Fig. S2, ESI†).[36] Both methods provide almost similar geometry parameters that are comparable to the X-ray results (Table 1). However, the optimized structure with B3LYP/SDD is more stable by 883.06 kcal mol^{-1} than B3LYP/LANL2DZ and hence shows relatively better agreement with the experimental results (Table 1), as reported for the related Pd(II)-complexes.[36b,36c] The excited state properties (*i.e.*, UV–vis. and ECD spectra) by TDDFT were calculated for the diastereomeric pair **Λ-[Pd(pic)*R*3]$^+$/Δ-[Pd(pic)*R*3]$^+$** and the enantiomeric pair **Λ-[Pd(pic)*R*3]$^+$/Λ-[Pd(pic)*S*3]$^+$** at B3LYP/SDD with the polarization continuum model (PCM) using dichloromethane as the solvent.[36] For calculations, 72 excited states (roots) were considered (Table S2, ESI†). The assignments on the UV–vis spectra and molecular orbitals (MOs) calculations were carried out at the same level of theory. The spectra were generated using the program SpecDis[47] by applying the Gaussian band shape with an exponential half-width of σ = 0.33 eV.

Biological evaluation

Stability studies. All compounds were studied for their stability in 100% DMSO-d6 by using NMR spectroscopy. Their ^{1}H-NMR spectra were recorded at time set intervals, over a period of 24 hours.

Cell lines and culture conditions

The MDA-MB-231 and MCF-7 breast cancer human tumour cells were purchased from ATCC. The MDA-MB-231 and MCF-7 cells were grown at 37 °C in 5% CO_2 in Dulbecco's modified Eagles's medium (DMEM high glucose) (Capricorn Scientific) or Dulbecco's modified Eagles's medium – DMEM (1X) + GlutaMAX (Gibco), respectively, supplemented with 10% fetal bovine serum (Capricorn Scientific). All cells were adherent in monolayers and, upon confluence, were washed with phosphate buffer saline (PBS) 1× and harvested by digestion with trypsin 0.05% (v/v). Trypsin was inactivated by adding fresh complete culture media to the culture flask. The cells were then suspended and transferred into new, sterile, culture flasks, or seeded in sterile test plates for different assays. All cells were manipulated under aseptic conditions in a flow chamber.

Compound dilution and storage

All compounds were dissolved in 100% DMSO, divided in aliquots of 100 μL each and stored at −20 °C until use.

Compound cytotoxicity evaluated using the MTT assay

The cells were adherent in monolayers and, upon confluency, were harvested by digestion with trypsin. The cytotoxicity of the complexes against the tumor cells was assessed using the colorimetric assay MTT (3-(4,5-2-yl)-2,5-ditetrazolium bromide),

which measures the conversion of the yellow tetrazolium into purple formazan by the mitochondrial redox activity in living cells. For this purpose, cells (10×10^3 or 20×10^3 in 200 μL of medium, for MDA-MB-231 or MCF-7, respectively) were seeded into 96-well plates and incubated in a 5% CO_2 incubator at 37 °C. The cells were settled for 24 h followed by the addition of a dilution series of the complexes in medium (200 μL). The complexes were first solubilized in 100% DMSO, given a 10 mM stock solution, and then in medium within the concentration range of 0.1–100 μM. DMSO did not exceed 1% even for the higher concentration used and was without cytotoxic effects. After 24 h of incubation, the treatment solutions were removed by aspiration, and MTT solution (200 μL, 0.5 mg mL^{-1} in PBS) was added to each well. After 3 h at 37 °C/5% CO_2, the solution was removed, and the purple formazan crystals formed inside the cells were dissolved in DMSO (200 μL) by thorough shaking. The cellular viability was evaluated by measuring the absorbance at 570 nm by using a microplate spectrophotometer.

Colony formation assay

The MDA-MB-231 cells were seeded in 12-well plates at 200 cells per mL. 24 hours after plating, the cells were incubated with 1/4 IC_{50} and IC_{50} values of the Pd(II) compounds. 24 hours after incubation, the old medium was removed, and the cells were incubated with a fresh medium. The medium was renewed every 3 days. 8 days after removing the treatments, the cells were washed with PBS and were incubated in a solution of glutaraldehyde (6% (v/v)) with crystal violet (0.5% (w/v)) for at least half an hour. The plate was washed with fresh water and left to air dry. Colonies were counted manually. The negative control was incubated with the corresponding volume of DMSO used in the solubilisation of the compounds (vehicle), and the final concentration of DMSO per well did not exceed 1%.

Cell death measurement using flow cytometry – the annexin V/PI assay

After a 24 h treatment with compounds **[Pd(pic)*R*2]NO_3**, **[Pd(pic)*S*2]NO_3**, **[Pd(pic)*R*6]NO_3**, **[Pd(pic)*S*6]NO_3**, **[Pd(pic)*R*7]NO_3** and **[Pd(pic)*S*7]NO_3**, both the suspended and attached cells were collected and washed with PBS. The cells were resuspended in 200 μL of 1× binding buffer and were incubated with 5 μL of FITC annexin V (BD Biosciences, San Jose, CA, USA) and 10 μL of PI (50 μg mL^{-1}) for 20 min in the dark. The samples were analysed by using fluorescence-activated cell sorting (FACS) using a Beckman Coulter EPICS XL-MCL. All data were analysed using the FlowJo software (version 10, Tree Star Inc.).

Conflicts of interest

There are no conflicts to declare.

Acknowledgements

The authors are grateful to the Research Council of the University of Isfahan (Iran) for the financial support of this work. Centro de Química Estrutural acknowledges Fundação para a Ciência e Tecnologia (FCT) for the Project UIDB/00100/2020. This work was also funded in the scope of the project PTDC/QUI-QIN/28662/2017 (FCT). A. Valente acknowledges the CEECIND 2017 Initiative (CEECIND/01974/2017). I. Correia acknowledges the program FCT Investigator (IF/00841/2012). We are grateful to Professor ABP Lever, Department of Chemistry, York University, Toronto and the Computecanada.ca (https://ccdb.computecanada.ca/) Ontario, Canada for using computational resources.

References

1 F. Arnesano, A. Pannunzio, M. Coluccia and G. Natile, *Coord. Chem. Rev.*, 2015, **284**, 286–297.
2 X. Zhao, S.-Q. Zang and X. Chen, *Chem. Soc. Rev.*, 2020, **49**, 2481–2503.
3 (*a*) Y. Wang, H. Huang, Q. Zhang and P. Zhang, *Dalton Trans.*, 2018, **47**, 4017–4026; (*b*) S. Zhang, X. Yao, N. H. Watkins, P. K. Rose, S. R. Caruso, C. S. Day and U. Bierbach, *Angew. Chem.*, 2020, **132**, 22149–22154; (*c*) M. Cini, T. D. Bradshaw, S. Woodward and W. Lewis, *Angew. Chem.*, 2015, **127**, 14385–14388.
4 L. Pendyala, Y. Kidani, R. Perez, J. Wilkes, R. Bernacki and P. Creaven, *Cancer Lett.*, 1995, **97**, 177–184.
5 (*a*) C.-H. Choi, Y.-J. Cha, C.-S. An, K.-J. Kim, K.-C. Kim, S.-P. Moon, Z. H. Lee and Y.-D. Min, *Cancer Cell Int.*, 2004, **4**, 1–12; (*b*) M. J. McKeage, *Expert Opin. Invest. Drugs*, 2001, **10**, 119–128.
6 (*a*) G. Gerebtzoff, X. Li-Blatter, H. Fischer, A. Frentzel and A. Seelig, *ChemBioChem*, 2004, **5**, 676–684; (*b*) M. Z. Hernandes, S. M. T. Cavalcanti, D. R. M. Moreira, W. F. de Azevedo Jr and A. C. L. Leite, *Curr. Drug Targets*, 2010, **11**, 303–314.
7 Z. Xu, Z. Yang, Y. Liu, Y. Lu, K. Chen and W. Zhu, *J. Chem. Inf. Model.*, 2014, **54**, 69–78.
8 R. Wilcken, M. O. Zimmermann, A. Lange, A. C. Joerger and F. M. Boeckler, *J. Med. Chem.*, 2013, **56**, 1363–1388.
9 P. Auffinger, F. A. Hays, E. Westhof and P. S. Ho, *Proc. Natl. Acad. Sci. U. S. A.*, 2004, **101**, 16789–16794.
10 (*a*) Y. Lu, T. Shi, Y. Wang, H. Yang, X. Yan, X. Luo, H. Jiang and W. Zhu, *J. Med. Chem.*, 2009, **52**, 2854–2862; (*b*) Q. Zhang, Z. Xu and W. Zhu, *J. Chem. Inf. Model.*, 2017, **57**, 22–26; (*c*) Z. Xu, Z. Liu, T. Chen, T. Chen, Z. Wang, G. Tian, J. Shi, X. Wang, Y. Lu and X. Yan, *J. Med. Chem.*, 2011, **54**, 5607–5611.
11 D. M. Himmel, K. Das, A. D. Clark, S. H. Hughes, A. Benjahad, S. Oumouch, J. Guillemont, S. Coupa, A. Poncelet and I. Csoka, *J. Med. Chem.*, 2005, **48**, 7582–7591.
12 Ö. Şahin, Ü. Ö. Özdemir, N. Seferoğlu, Z. K. Genc, K. Kaya, B. Aydıner, S. Tekin and Z. Seferoğlu, *J. Photochem. Photobiol., A*, 2018, **178**, 428–439.
13 (*a*) D. Gutiérrez, S. Bernès, G. Hernández, O. Portillo, G. E. Moreno, M. Sharma, P. Sharma and R. Gutiérrez,

J. Coord. Chem., 2015, **68**, 3805–3813; (*b*) T. Lazarević, A. Rilak and Ž. D. Bugarčić, *Eur. J. Med. Chem.*, 2017, **142**, 8–31; (*c*) A. R. Khohkar, Q. Xu and Z. H. Siddik, *J. Inorg, Biochem.*, 1990, **39**, 117–123; (*d*) A. R. Khohkar and G. J. Lumetta, *J. Coord. Chem.*, 1989, **19**, 321–330; (*e*) C. Cullinane, G. B. Deacon, P. Drago, A. Erven, P. C. Junk, J. Luu, G. Meyer, S. Schmitz, I. Ott, J. Schur, L. Webster and A. Klein, *Dalton Trans.*, 2018, **18**, 1918–1932; (*f*) V. Lingen, A. Lüning, A. Krest, G. B. Deacon, J. Schur, I. Ott, I. Pantenburg, G. Meyer and A. Klein, *J. Inorg. Chem.*, 2016, **165**, 119–125; (*g*) C. G. Oliveira, I. Romero-Canelón, M. M. Silva, J. P. C. Coverdale, P. I. S. Maia, A. A. Batista, S. Castelli, A. Desideri, P. J. Sadler and V. M. Deflon, *Dalton. Trans.*, 2019, **48**, 16509–16517; (*h*) C. G. Oliveira, I. Romero-Canelón, J. P. C. Coverdale, P. I. S. Maia, G. J. Clarkson, V. M. Deflon and P. J. Sadler, *Dalton. Trans.*, 2020, **49**, 9595–9604.

14 Ž. D. Bugarčić, J. Bogojeski and R. van Eldik, *Coord. Chem. Rev.*, 2015, **292**, 91–106.

15 (*a*) A. I. Matesanz, E. Jimenez-Faraco, M. C. Ruiz, L. M. Balsa, C. Navarro-Ranninger, I. E. León and A. G. Quiroga, *Inorg. Chem. Front.*, 2018, **5**, 73–83; (*b*) M. D. Coskun, F. Ari, A. Y. Oral, M. Sarimahmut, H. M. Kutlu, V. T. Yilmaz and E. Ulukaya, *Biorg. Med. Chem.*, 2013, **21**, 4698–4705.

16 (*a*) A. Kumar, A. Naaz, A. Prakasham, M. K. Gangwar, R. J. Butcher, D. Panda and P. Ghosh, *ACS Omega*, 2017, **2**, 4632–4646; (*b*) A. S. Abu-Surrah, T. A. Al-Allaf, L. J. Rashan, M. Klinga and M. Leskelä, *Eur. J. Med. Chem.*, 2002, **37**, 919–922.

17 G. G. Mohamed, M. M. Omar and A. M. Hindy, *Turk. J. Chem.*, 2006, **30**, 361–382.

18 (*a*) L. H. Abdel-Rahman, M. S. S. Adam, A. M. Abu-Dief, H. Moustafa, M. T. Basha, A. S. Aboraia, B. S. Al-Farhan and H. E. S. Ahmed, *Appl. Organomet. Chem.*, 2018, **32**, e4527; (*b*) Z. Faghih, A. Neshat, A. Wojtczak, Z. Faghih, Z. Mohammadi and S. Varestan, *Inorg. Chim. Acta*, 2018, **471**, 404–412.

19 M. S. Iqbal, S. J. Khurshid and B. Muhammad, *Med. Chem. Res.*, 2013, **22**, 861–868.

20 (*a*) C. Satheesh, P. R. Kumar, P. Sharma, K. Lingaraju, B. Palakshamurthy and H. R. Naika, *Inorg. Chim. Acta*, 2016, **442**, 1–9; (*b*) E. Yousif, A. Majeed, K. Al-Sammarrae, N. Salih, J. Salimon and B. Abdullah, *Arabian J. Chem.*, 2017, **10**, S1639–S1644.

21 L. Wei, W. Tan, G. Wang, Q. Li, F. Dong and Z. Guo, *Carbohydr. Polym.*, 2019, **226**, 115256.

22 (*a*) Z. Kazemi, H. A. Rudbari, M. Sahihi, V. Mirkhani, M. Moghadam, S. Tangestaninejad, I. Mohammadpoor-Baltork, G. Azimi, S. Gharaghani and A. A. Kajani, *J. Photochem. Photobiol., A*, 2016, **163**, 246–260; (*b*) Z. Kazemi, H. A. Rudbari, V. Mirkhani, M. Sahihi, M. Moghadam, S. Tangestaninejad, I. Mohammadpoor-Baltork, A. A. Kajani and G. Azimi, *Eur. J. Med. Chem.*, 2017, **135**, 230–240.

23 N. Kordestani, H. A. Rudbari, G. Bruno, R. Scopelliti, J. D. Braun, D. E. Herbert, O. Blacque, I. Correia, M. A.-M. Zaman and M. M. Bindu, *Dalton Trans.*, 2020, **50**, 3990–4007.

24 M. Van Beusichem and N. Farrell, *Inorg. Chem.*, 1992, **31**, 634–639.

25 G. Y. Park, J. J. Wilson, Y. Song and S. J. Lippard, *Proc. Natl. Acad. Sci. U. S. A.*, 2012, **109**, 11987–11992.

26 (*a*) M. Khorshidifard, H. A. Rudbari, Z. Kazemi-Delikani, V. Mirkhani and R. Azadbakht, *J. Mol. Struct.*, 2015, **1081**, 494–505; (*b*) M. Khorshidifard, H. A. Rudbari, B. Askari, M. Sahihi, M. R. Farsani, F. Jalilian and G. Bruno, *Polyhedron*, 2015, **95**, 1–13.

27 (*a*) N. Karayannis, C. Mikulski, M. Strocko, L. Pytlewski and M. Labes, *Inorg. Chim. Acta*, 1974, **8**, 91–96; (*b*) C. Addison and N. Logan, *Q. Rev., Chem. Soc.*, 1971, **25**, 289.

28 H. Flack, *Acta Crystallogr., Sect. A: Found. Crystallogr.*, 1983, **9**, 876–881.

29 (*a*) M. Enamullah, A. R. Uddin, G. Pescitelli, R. Berardozzi, G. Makhloufi, V. Vasylyeva, A.-C. Chamayou and C. Janiak, *Dalton Trans.*, 2014, **43**, 3313–3329; (*b*) M. Enamullah, M. A. Quddus, M. R. Hasan, G. Pescitelli, R. Berardozzi, G. Makhloufi, V. Vasylyeva and C. Janiak, *Dalton Trans.*, 2016, **45**, 667–680; (*c*) M. Enamullah, M. A. Quddus, M. M. Rahman and T. E. Burrow, *J. Mol. Struct.*, 2017, **1130**, 765–774.

30 (*a*) M. Enamullah, G. Makhloufi, R. Ahmed, B. A. Joy, M. A. Islam, D. Padula, H. Hunter, G. Pescitelli and C. Janiak, *Inorg. Chem.*, 2016, **55**, 6449–6464; (*b*) G. Pescitelli, S. Lüdeke, A.-C. Chamayou, M. Marolt, V. Justus, M. Górecki, L. Arrico, L. D. Bari, M. A. Islam and I. Gruber, *Inorg. Chem.*, 2018, **57**, 1339–1340; (*c*) M. Enamullah, V. Vasylyeva, M. A. Quddus, M. K. Islam, S.-P. Höfert and C. Janiak, *CrystEngComm*, 2018, **20**, 4724–4734.

31 (*a*) M. Enamullah, M. A. Quddus, M. R. Hasan, G. Pescitelli, R. Berardozzi, G. J. Reiß and C. Janiak, *Eur. J. Inorg. Chem.*, 2015, 2758–2768; (*b*) M. Enamullah, M. A. Islam, B. A. Joy, B. Dittrich, G. J. Reiss and C. Janiak, *Inorg. Chim. Acta*, 2018, **482**, 935–942.

32 (*a*) T. Al-Allaf, P. Castan, R. Turpin, S. Wimmer and G. Bernardinelli, *Transition Met. Chem.*, 1992, **17**, 579–582; (*b*) M. B. Smith and A. M. Slawin, *Polyhedron*, 2000, **19**, 695–704; (*c*) T. Tsuno, H. Iwabe and H. Brunner, *Inorg. Chim. Acta*, 2013, **400**, 262–266.

33 T. Rau, M. Shoukry and R. van Eldik, *Inorg. Chem.*, 1997, **36**, 1454–1463.

34 J. Bernstein, *Angew. Chem., Int. Ed. Engl.*, 1995, **34**, 1555–1573.

35 C. F. Mackenzie, P. R. Spackman, D. Jayatilaka and M. A. Spackman, *IUCrJ*, 2017, **4**, 575–587.

36 (*a*) G. Yang, C. Jin, J. Hong, Z. Guo and L. Zhu, *Spectrochim. Acta, Part A*, 2004, **60**, 3187–3195; (*b*) S. Mukherjee, S. Chowdhury, A. P. Chattapadhyay and A. Bhattacharya, *Inorg. Chim. Acta*, 2011, **373**, 40–46; (*c*) L. Zhang, Y. Zhang, H. Tao, X. Sun, Z. Guo and L. Zhu, *J. Mol. Struct.*, 2002, **617**, 87–97; (*d*) S. Mukherjee, S. Chowdhury, A. P. Chattopadhyay and H. Stoeckli-Evans, *Polyhedron*, 2010, **29**, 1182–1188; (*e*) S. Chakrabarty, S. Bhattacharjee, R. Rahmani, A. H. Sheikh, A. Chouaih, F. Hamzaoui, F. A. Akbari and Z. Alinia, *Turk. J. Chem.*, 2013, 37.

37 (*a*) W. Lu, B.-X. Mi, M. C. Chan, Z. Hui, C.-M. Che, N. Zhu and S.-T. Lee, *J. Am. Chem. Soc.*, 2004, **126**, 4958–4971; (*b*) J. G. Williams, *Photochem. Photophysics. Coord. Comp.*, 2007, 205–268.
38 (*a*) A. Garoufis, S. Hadjikakou and N. Hadjiliadis, *Coord. Chem. Rev.*, 2009, **253**, 1384–1397; (*b*) M. Vojtek, M. P. Marques, I. M. Ferreira, H. Mota-Filipe and C. Diniz, *Drug Discovery Today*, 2019, **24**, 1044–1058.
39 L. Côrte-Real, B. Karas, P. Gírio, A. Moreno, F. Avecilla, F. Marques, B. T. Buckley, K. R. Cooper, C. Doherty and P. Falson, *Eur. J. Med. Chem.*, 2019, **163**, 853–863.
40 Bruker, *APEX3, SAINT and SADABS*. Bruker AXS Inc., Madison, Wisconsin, USA, 2017.
41 G. M. Sheldrick, *Acta Crystallogr., Sect. A: Found. Crystallogr.*, 2008, **64**, 112.
42 A. Spek, *Acta Crystallogr., Sect. D: Biol. Crystallogr.*, 2009, **65**, 148–155.
43 P. CrysAlis, Yarnton, England, 2009.
44 O. V. Dolomanov, L. J. Bourhis and R. J. Gildea, *J. Appl. Crystallogr.*, 2009, **42**, 339–341.
45 G. M. Sheldrick, *Acta Crystallogr., Sect. C: Struct. Chem.*, 2015, **71**, 3–8.
46 M. Frisch, F. Clemente, Scalmani, V. Barone, B. Mennucci, G. A. Petersson, H. Nakatsuji, M. Caricato, X. Li, H. P. Hratchian, A. F. Izmaylov, J. Bloino and G. Zhe.
47 T. Bruhn, A. Schaumlöffel, Y. Hemberger and G. Bringmann, *Chirality*, 2013, **25**, 243–249.

